# Laser-probe $^{40}$Ar/$^{39}$Ar dating of strain fringes: Mid-Cretaceous synconvergent orogen-parallel extension in the interior of the Sevier orogen

Michael L. Wells,[1] Terry L. Spell,[1] Thomas D. Hoisch,[2] Tonia Arriola,[1] and Kathleen A. Zanetti[1]

[1] UV and $CO_2$ laser-probe $^{40}$Ar/$^{39}$Ar in situ analyses of phlogopite and muscovite in fibrous strain fringes from greenschist-facies metamorphic rocks document mica growth ages at temperatures lower than their closure temperatures, and therefore directly date deformation. The new dates resolve the age of the earliest ductile fabric recorded in the Raft River–Albion–Grouse Creek metamorphic core complex of Utah and Idaho. Phlogopite was dated in quartz-calcite-phlogopite strain fringes around pyrite in Pennsylvanian-Permian rocks from the Grouse Creek Mountains (Utah) using both the UV and $CO_2$ laser probe; muscovite was dated in quartz-muscovite strain fringes around pyrite in deformed Jurassic sills from the Black Pine Mountains (Idaho) using the $CO_2$ laser probe. Phlogopite $^{40}$Ar/$^{39}$Ar ages for individual strain fringes (Grouse Creek Mountains) range from 92 Ma to 110 Ma, with the most reliable ages ranging from 101 Ma to 110 Ma (mean age, 105.0 ± 5.8 Ma). Muscovite $^{40}$Ar/$^{39}$Ar ages for individual strain fringes (Black Pine Mountains) range from 97 Ma to 112 Ma (mean age, 104.7 ± 5.8 Ma). Strain fringes are associated with a subhorizontal foliation and a generally N-trending elongation lineation exhibiting components of top-to-the-north simple shear and coaxial strain accommodating N-S extension and subvertical shortening. Midcrustal northward flow at 105 (±6) Ma within the interior of the Sevier orogen, coeval with east-directed shortening in the foreland and with plate convergence, records orogen-parallel synconvergent extension. We favor gravitational relaxation of structural culminations resulting from focused crustal shortening as a driving mechanism for orogen-parallel flow. **Citation:** Wells, M. L., T. L. Spell, T. D. Hoisch, T. Arriola, and K. A. Zanetti (2008), Laser-probe $^{40}$Ar/$^{39}$Ar dating of strain fringes: Mid-Cretaceous synconvergent orogen-parallel extension in the interior of the Sevier orogen, *Tectonics*, *27*, TC3012, doi:10.1029/2007TC002153.

## 1. Introduction

[2] Determining the absolute ages of deformation fabrics in metamorphic rocks is critical to understanding the nature of orogenesis in deeply exhumed ancient mountain belts. For example, ages are necessary for establishing rates and durations of deformation processes and the timing of important kinematic transitions such as from shortening to extension. Dating minerals that grew during deformation (syntectonic minerals) is especially useful, because of the potential to directly link the isotopic age to the deformation fabric. Syntectonic minerals will yield the age of deformation when isotopic closure temperatures ($T_c$) are higher than crystallization temperatures [e.g., *Getty and Gromet*, 1992; *Müller et al.*, 2000; *Sherlock et al.*, 2003]. Direct dating of syntectonic minerals requires adequate characterization of: (1) the appropriate $T_c$ for the mineral phase and grain size, (2) the temperature of growth during deformation and metamorphism and, (3) the textural relationships between mineral phases and deformation fabrics [*Dunlap*, 1997; *Reddy and Potts*, 1999; *Müller*, 2003; *Mulch and Cosca*, 2004]. In situ isotopic analysis provides a critical advantage over bulk analysis of mineral separates because the relationships between the analyzed mineral, deformation fabric, and age, can be directly studied [*Müller et al.*, 2000], thus eliminating potential complications of dating mixtures of mineral grains of different age and textural affinity. Dating minerals in fibrous strain fringes is particularly advantageous because mineral growth can be clearly linked to the progressive incremental strain history [*Ramsay and Huber*, 1983; *Koehn et al.*, 2000; *Müller et al.*, 2000].

[3] Here we apply in situ $^{40}$Ar/$^{39}$Ar UV and $CO_2$ laser techniques to dating phlogopite in quartz-phlogopite-calcite and muscovite in quartz-muscovite fibrous strain fringes in greenschist-facies metamorphic rocks. To our knowledge, these are the first successful applications of the laser probe to in situ $^{40}$Ar/$^{39}$Ar dating of fibrous strain fringes. In both cases, syntectonic mica growth occurred below the minerals $T_c$ and thus the ages represent the timing of growth and deformation. The new dates yield a mid-Cretaceous age for the earliest ductile fabric ($D_1$) preserved in the Raft River–Albion–Grouse Creek metamorphic core complex of Utah and Idaho, in the interior (hinterland) of the retroarc Sevier orogenic belt. When combined with observations of the $D_1$

[1]Department of Geoscience, University of Nevada, Las Vegas, Nevada, USA.

[2]Department of Geology, Northern Arizona University, Flagstaff, Arizona, USA.

fabric and geophysical constraints on relative plate motions, these data lead to a reinterpretation of the tectonic significance of the $D_1$ fabric as recording a previously unrecognized period of synconvergent orogen-parallel extensional flow during dominantly orthogonal plate convergence. Synconvergent orogen-parallel extension, common in the interiors of orogenic belts worldwide [e.g., *Ellis and Watkinson*, 1987; *Mancktelow*, 1992; *McCaffrey*, 1992; *Murphy et al.*, 2002], is most commonly interpreted within the contexts of transpression, arcuation, or indentation and lateral escape. We suggest an alternative interpretation for the cause of some occurrences of synconvergent orogen-parallel extension as gravitational relaxation due to unequal crustal thickening along orogenic strike.

## 2. Structural Setting

[4] Midcrustal levels of the interior of the Jurassic to Early Eocene Cordilleran (Sevier) orogenic belt are exposed within the footwalls of some Cenozoic detachment faults in the Great Basin, for example within the Snake Range, the Ruby Mountains–East Humboldt Range–Wood Hills area, and the Raft River–Albion–Grouse Creek Mountains (Figure 1). These exposures record deformation processes within deep levels of a retroarc noncollisional orogen. The recorded events include substantial crustal thickening, thrust burial metamorphism, and extensional exhumation broadly synchronous with thrusting in the external fold-thrust belt [*Camilleri and Chamberlain*, 1997; *Wells*, 1997; *McGrew et al.*, 2000; *Hoisch et al.*, 2002; *DeCelles*, 2004; *Harris et al.*, 2007]. An understanding of the deformation history of these rocks is important, not only to better understand the Cordilleran orogen, but also in moving toward a more complete understanding of retroarc noncollisional fold-thrust belts in general, as these rocks are often considered a more deeply exhumed analog to the modern Andean mountain belt [e.g., *Jordan et al.*, 1983].

[5] The Raft River, Albion, Grouse Creek and Black Pine Mountains comprise an extensive metamorphic core complex that exposes Proterozoic to Triassic metasedimentary rocks, which unconformably overlie Archean basement [*Armstrong*, 1968; *Compton et al.*, 1977; *Wells*, 1997] (Figure 2). The stratigraphic section and metamorphic isograds have been greatly condensed by plastic attenuation and omission of stratigraphy along Mesozoic and Cenozoic low-angle normal faults and shear zones [*Wells*, 1997].

## 3. $D_1$ Fabric Distribution, Orientation, and Kinematics

### 3.1. Raft River–Albion–Grouse Creek Mountains

[6] The oldest deformation fabric ($D_1$) in the Raft River–Albion–Grouse Creek metamorphic core complex exhibits a flat-lying foliation ($S_1$) and generally north-trending elongation lineation ($L_1$) and has been described in the Albion [*Armstrong*, 1968; *Miller*, 1980; *Wells*, 1997], Grouse Creek [*Compton et al.*, 1977; *Todd*, 1980; *Malavieille*, 1987; *Sheely*, 2002] and Raft River Mountains [*Compton et al.*,

1977; *Wells et al.*, 1990, 1997] (Figure 2). $L_1$ is parallel to locally developed intersection lineations and $F_1$ hingelines [*Compton et al.*, 1977; *Miller*, 1980; *Todd*, 1980; *Malavieille*, 1987] (Figure 2). The $D_1$ fabric is expressed locally in the Archean to Proterozoic parautochthon (Figure 3d) and several overlying allochthons bounded by low-angle normal faults of both Cenozoic and Mesozoic age, including the Oligocene–late Miocene Raft River detachment and Eocene–early Miocene Middle detachment. Despite maximum differences in the azimuth of $L_1$ as great as 60° across contiguous exposures of the parautochthon and between allochthons and the parautochthon (Figure 2), $D_1$ fabrics are correlated throughout the Raft River, Albion, and Grouse Creek Mountains on the basis of similarity in deformation kinematics and structural sequence [*Compton et al.*, 1977; *Todd*, 1980; *Malavieille*, 1987; *Wells et al.*, 1997]. The $D_1$ fabric is evident in Archean to Ordovician rocks where the Cenozoic extensional strain overprint is not strong (Figures 2 and 3), and important to this study, in the structurally higher Mississippian to Permian rocks of the middle allochthon in the Grouse Creek Mountains (Figures 3a–3c) and Devonian to Permian rocks of the nearby Black Pine Mountains. The $D_1$ fabric is not developed in the middle allochthon of the Raft River or Albion Mountains; in these areas, the rocks of the middle allochthon are not penetratively deformed.

[7] Kinematic studies of $D_1$ shearing in Archean to Permian rocks indicate top-to-north noncoaxial shear (Figure 3a) with a significant component of pure shear, the latter of which accomplishes layer-parallel extension and layer-perpendicular shortening [*Malavieille*, 1987; *Wells*, 1997; *Sheely*, 2002] (Figure 3). Finite strain magnitudes, based primarily on qualitative observations, are heterogeneous both laterally and vertically and high strain zones dominated by simple shear deformation are common at lithologic boundaries. Proterozoic and Ordovician metasedimentary strata, where not affected by younger penetrative strain, exhibit $S_1$ foliation parallel to lithologic layering and substantial attenuation of rock units [*Compton et al.*, 1977; *Todd*, 1980; *Malavieille*, 1987; *Wells*, 1997].

[8] Previous geochronology investigations have established a Late Cretaceous or older age for $D_1$ fabric development. Late Cretaceous K-Ar ages (biotite, muscovite, and hornblende) have been reported from lower amphibolite facies rocks containing $L_1$ lineation from the northern Albion Mountains [*Armstrong*, 1976; *Miller*, 1980]. Three $^{40}Ar/^{39}Ar$ muscovite analyses from uppermost greenschist-facies Ordovician marble and schist containing $D_1$ fabrics in the eastern Raft River Mountains yielded 88–90 Ma cooling ages [*Wells et al.*, 1990]. The $D_1$ fabrics are interpreted to have developed prior to cooling at ~90 Ma on the basis of deformation mechanisms that indicate temperatures higher than the Ar closure temperatures. In consideration of regional tectonic relations [e.g., *DeCelles*, 2004], this leaves open a range of possible ages for $D_1$ fabrics from Late Jurassic to mid-Cretaceous.

### 3.2. Black Pine Mountains

[9] Greenschist-facies Devonian to Permian rocks in the Black Pine Mountains, which occur in several stacked
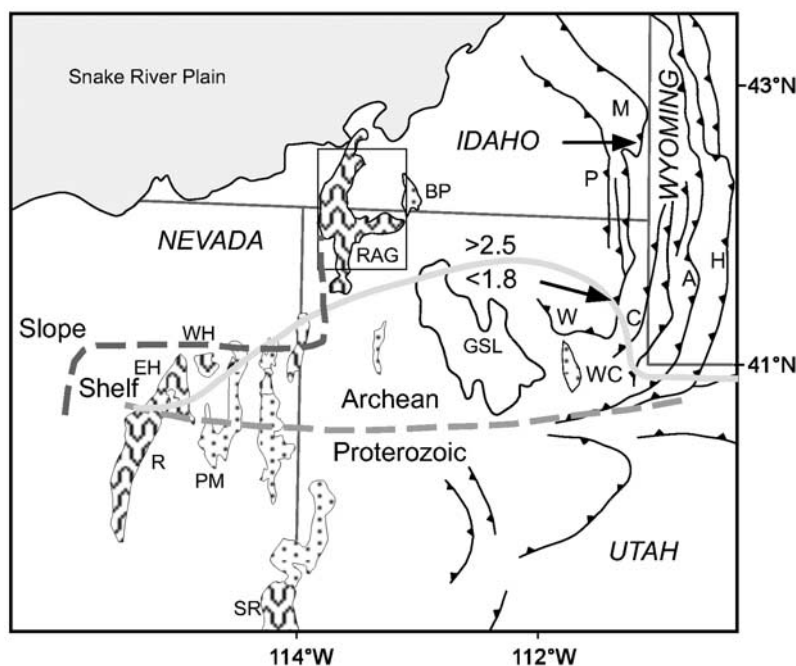
**Figure 1.** Location map of Raft River–Albion–Grouse Creek metamorphic core complex, within the hinterland of the Sevier fold-thrust belt. Lower grade metamorphic rocks shown in stippled pattern include: BP, Black Pine; PM, Pequop; higher-grade metamorphic rocks shown in wavy line pattern include: R, Ruby Mountains; EH, East Humboldt Range; WH, Wood Hills; SR, Snake Range; and RAG, Raft River, Albion, Grouse Creek Mountains. Traces of major thrusts of the fold-thrust belt include: W, Willard; P, Paris; M, Meade; C, Crawford; A, Absaroka; H, Hogsback. WC is Wasatch basement culmination. Arrows indicate estimates for thrust transport direction from *Royse* [1993] and *Yonkee* [1997]. Inferred positions of Precambrian crustal boundary shown by light gray dashed line, modified from *Bryant* [1988] and *Lush et al.* [1988], and by gray solid line after *Nelson et al.* [2002], modified from *Zartman* [1974]. Early Paleozoic shelf-slope break from *Miller et al.* [1991].

low-angle fault-bounded allochthons, exhibit a foliation previously correlated to $S_1$ of the Raft River–Albion–Grouse Creek metamorphic core complex on the basis of similarity in structural sequence [*Wells and Allmendinger*, 1990; *Wells et al.*, 1990]. The strain significance of this fabric is best understood from studying carbonate rocks in the Pennsylvanian-Permian Oquirrh and Devonian Guilmette Formations in low-angle fault contact above and below, respectively, an allochthon of Upper Pennsylvanian and Lower Mississippian Manning Canyon Shale. Vorticity and finite strain studies of the $D_1$ fabric in the carbonate rocks document up to 160% layer-parallel extension, layer-perpendicular shortening, plane strain, and a coaxial strain path [*Wells and Allmendinger*, 1990]. An ~E-W extension direction is reconstructed for the Devonian to Permian rocks by consideration of a variety of features including folded and boudinaged calcite and quartz veins in the Oquirrh Formation; vein fibers and strain fringes in the Oquirrh Formation, Manning Canyon Shale and associated Jurassic sills; and stretching lineations which are most prominent in the Devonian marble (Figure 2). This event is associated with synkinematic metamorphism and growth of white mica along slaty cleavage in the siltites and slates of the Manning Canyon Shale.

[10] Previous geochronology studies have suggested a mid-Cretaceous age for metamorphism and cleavage formation. *Smith* [1982] reported nine K-Ar whole rock slate ages of 77 to 111 Ma. *Wells et al.* [1990] reported four discordant whole-rock $^{40}Ar/^{39}Ar$ age spectra with variable total gas ages from 168 to 93 Ma. On the basis of a relationship of decreasing discordancy and total gas age correlating with increasing structural depth, increasing cleavage intensity, and increasing proportion of neoblastic syncleavage white mica relative to detrital white mica, the two mid-Cretaceous ages (93.4 ± 5.9 Ma and 101.1 ± 1.6 Ma) from the structurally deepest level were interpreted to record the age of metamorphism and cleavage formation [*Wells et al.*, 1990].

## 4. D$_1$ Strain Fringes

### 4.1. Grouse Creek Mountains

[11] In the Grouse Creek Mountains, the $D_1$ fabric is well preserved structurally above the Cenozoic Middle detachment fault within the Pennsylvanian-Permian Oquirrh Formation of the middle allochthon (Figure 2). The fabrics have been mapped in many exposures of Oquirrh Formation in the Grouse Creek Mountains [*Compton et al.*, 1977;
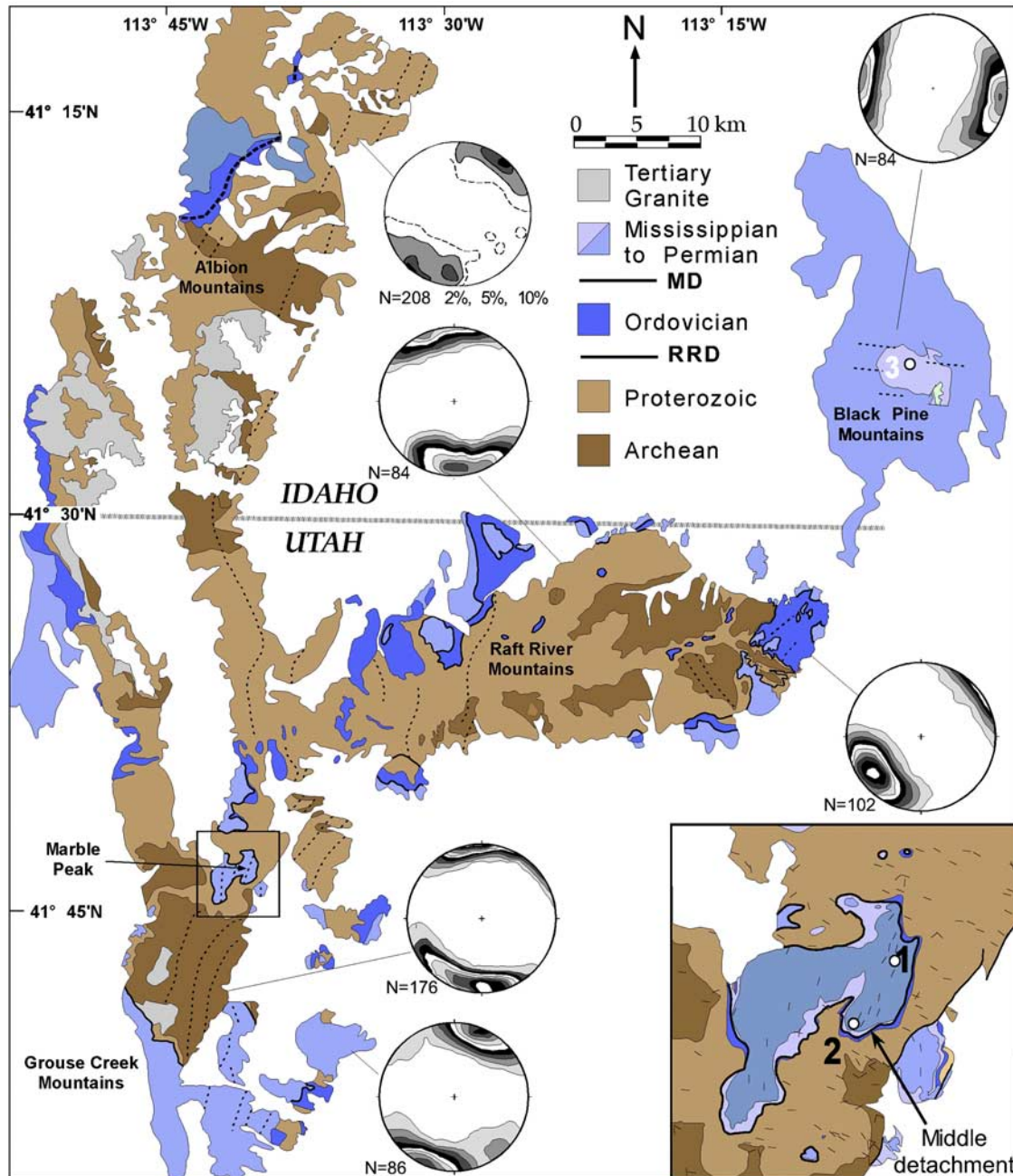
**Figure 2.** Generalized geologic map of Raft River–Albion–Grouse Creek metamorphic core complex showing distribution and orientation of the $L_1$ stretching lineation. Lineation measurements used to construct stereograms of $L_1$ from *Compton* [1972, 1975], *Miller* [1980], *Todd* [1980], *Sheely* [2002], *Wells* [1997], and unpublished data of M.L.W. (2000 and 2003) and T.A. [2006]. Stereograms with contour intervals of $2\sigma$ with exception of northernmost (Albion) shown at 2%, 5%, 10% per 1% area. Inset is detail of the Marble Peak klippe showing preservation of $L_1$ lineation above Middle detachment and sample localities of strain fringes: location 1, sample used for UV laser probe and step-heating analysis; location 2, sample used for $CO_2$ laser-probe analyses. Note that locations 1 and 2 are ~150 m and ~15 m above the Middle detachment, respectively.

*Todd*, 1980] but here we focus on the Marble Peak klippe, the site of our $^{40}Ar/^{39}Ar$ geochronology study (Figure 2). Fibrous strain fringes developed adjacent to 2–10 mm pyrite porphyroblasts within calcareous metasiltstones define

a NNE-trending elongation lineation (Figures 2 and 3), parallel to an intersection lineation and indicate variable maximum finite extensions of 60 to 150%. The strain fringes record two growth events. The younger growth
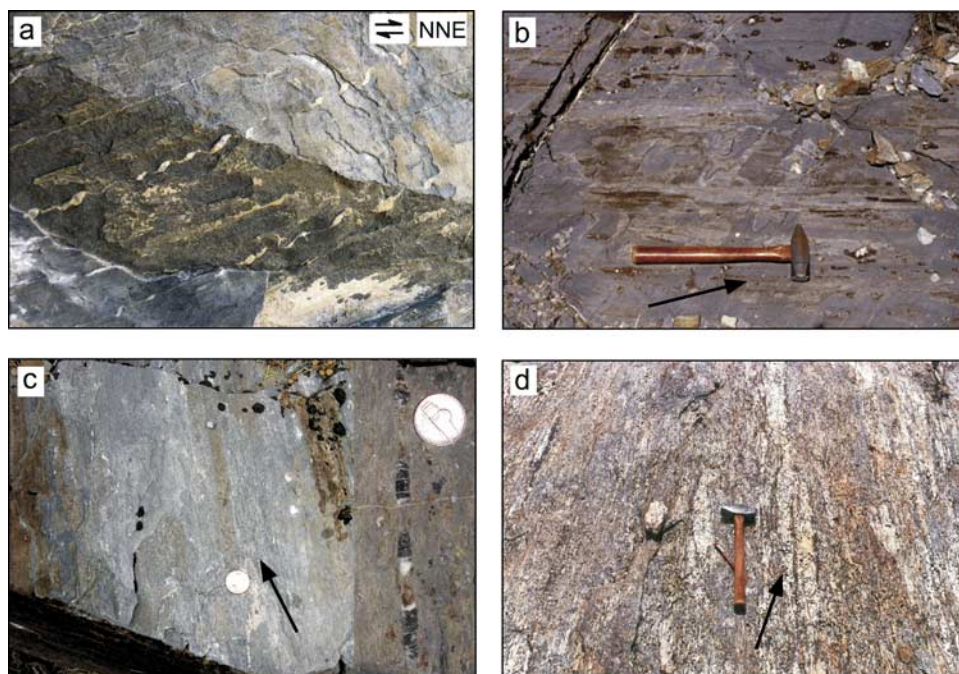
**Figure 3.** Field photographs of $D_1$ fabrics in the Grouse Creek Mountains. (a) Asymmetric boudinage of quartz veins in Oquirrh Formation marble, showing top-to-NNE shear. (b, c), Stretching lineation in Oquirrh Formation marble. Inset in Figure 3c is stretched crinoid stem (black), pull-aparts infilled by quartz and calcite. (d) Strong N-trending stretching lineation in Archean orthogneiss. Arrows on Figures 3b–3d indicate north direction.

event is recorded as thin (width $1-12$ $\mu$m) quartz fibers that postdate $D_1$ fiber growth (Figure 4a). The older fibers ($D_1$) are face-controlled, antitaxial, and consist of quartz, calcite, and phlogopite (Figure 4). The optical continuity in quartz and calcite between matrix grains and fibers within the strain fringe indicates fiber growth from matrix toward pyrite (Figure 4c), consistent with the pyrite-type strain fringe growth model [*Ramsay and Huber*, 1983; *Koehn et al.*, 2000]. In some strain fringes (Figure 4a) phlogopite crystals are discordant to face-controlled quartz fibers and appear displacement-controlled, similar in orientation to "ghost" fibers [*Ramsay and Huber*, 1983]. Phlogopite fibers exhibit $c$ axes oriented parallel to fiber length (i.e., approximately perpendicular to pyrite faces), and are mostly of uniform crystallographic orientation. Exceptions are in local zones exhibiting postgrowth intracrystalline strain including kink bands and intragranular fractures. The outlines of $D_1$ strain fringes in XZ planes (finite strain ellipsoid) are oblique to the dominant foliation ($S_1$) and internally asymmetric (Figure 4a) and indicate noncoaxial top-to-northeast shear [e.g., *Koehn et al.*, 2000]. Further south in the Grouse Creek Mountains, strain fringes within the Oquirrh Formation are more asymmetric and apparently record a larger component of top-to-north simple shear [*Malavieille*, 1987].

### 4.2. Black Pine Mountains

[12] Sparse intermediate composition dikes and sills intrude the Upper Mississippian and the Lower Pennsylvanian Manning Canyon Shale in the Black Pine Mountains [*Smith*, 1982; *Wells et al.*, 1990]. The intrusions are altered and cleaved, and at one locality pyrite ($1-2$ cm) is abundant within a sill and in the adjacent siltite and slate country rock. The sill shows a gradation from an interior of fresher and less cleaved rock to a more altered and cleaved margin. Quartz-muscovite strain fringes around pyrite are abundant in both country rock and sill; the strain fringes are larger and record more strain in the altered sill near the margin, where the pyrite is mostly altered to goethite. The rubbly outcrop habit of the sill and the large size of the strain fringes preclude a detailed strain study, however, a few measurements indicate variable extension magnitudes from $50-90\%$, lower than the measured strain values in the Oquirrh Formation [*Wells and Allmendinger*, 1990]. Examination of in-place siltite and slate country rock shows a strain fringe orientation compatible with that of the slaty cleavage, and bulk extension oriented east-west, similar to that described by *Wells and Allmendinger* [1990] from the overlying Oquirrh Formation. Quartz and muscovite are intimately intergrown throughout the strain fringes at the micron scale and muscovite forms larger fibrous composite grains at the millimeter scale (Figure 5). Distal fringe material (near the matrix) tends to be dominantly muscovite.

## 5. The $^{40}$Ar/$^{39}$Ar Experimental Methods

[13] Samples of the Oquirrh Formation containing $D_1$ strain fringes were collected from two locations within the
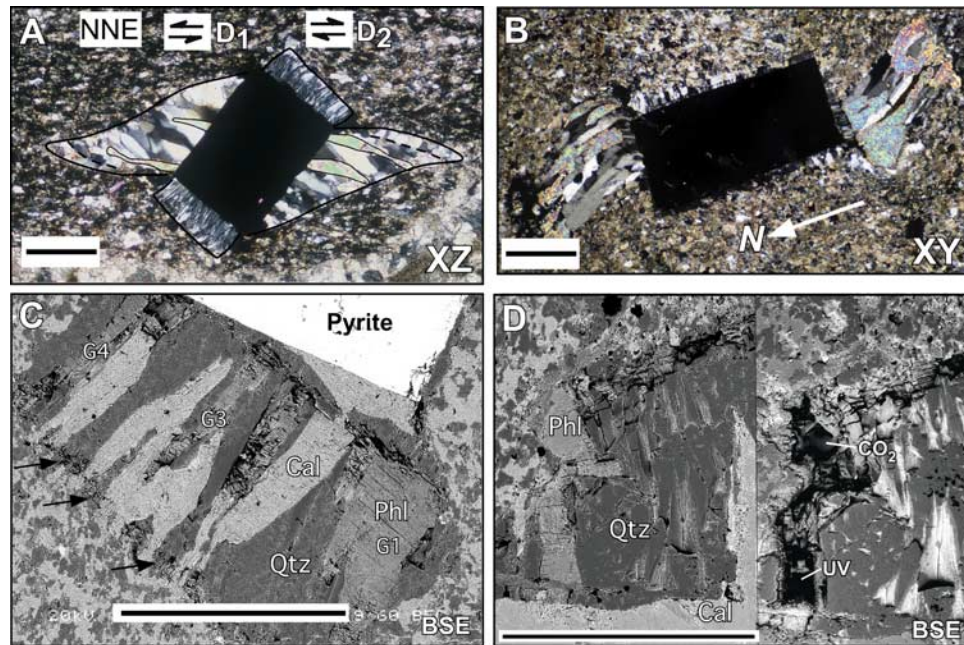
**Figure 4.** Images of $D_1$ strain fringes from sample 1. (a) Photomicrograph (PL) of two generations of strain fringe growth. First generation ($D_1$) fibers consist of quartz, calcite, and phlogopite (outlined). Suture between face-controlled quartz fibers shown by dashed line. Note that phlogopite fibers are displacement controlled, and discordant to face-controlled quartz fibers. Trace of $S_1$ foliation is horizontal, XZ plane of finite strain ellipsoid. (b) Photomicrograph of quartz-phlogopite strain fringe from sample 2 within the plane of foliation (XY plane of finite strain ellipsoid). (c) scanning electron microscope (SEM), back-scattered electron (BSE) image of strain fringe. Note continuity in quartz (arrows) and calcite between matrix and fibers. Phlogopite fibers labeled G1, G3, and G4 were analyzed by the UV laser probe. Phl, phlogopite; Qtz, quartz; Cal, Calcite. (d) SEM BSE images of phlogopite fiber F analyzed by UV and $CO_2$ laser: left-hand image is prior to analysis; right-hand image shows fiber excavation by UV laser and subsequent melting by $CO_2$ laser. Scale bars are 1 mm in length.

Marble Peak klippe; sample 1, ~150 m, and sample 2, ~15 m above the Middle detachment, respectively (Figure 2). Eight thick sections (chips) with dimensions of ~100 mm² by 3 mm thick containing pyrite porphyroblasts and both sides of fibrous strain fringes were prepared and polished for each of the two samples. A mineral separate of muscovite from the matrix of both samples 1 and 2 was also prepared.

[14] Samples of a cleaved sill containing quartz-muscovite strain fringes around pyrite, and of the surrounding contact-metamorphosed siltite of the Manning Canyon Shale, were collected from the Black Pine Mountains. Nine thick sections (chips) with dimensions of ~225 mm² by 3 mm thick, each containing one side of a fibrous strain fringe were prepared and polished. A mineral separate of muscovite from the contact aureole in the Manning Canyon Shale was also prepared.

[15] Thick sections were imaged and characterized by scanning electron microscopy and electron microprobe analysis in the Electron Microanalysis and Imaging Laboratory (EMIL) at UNLV using a JEOL-8900 electron probe microanalyzer and JEOL-5600 scanning electron microscope. Electron microprobe analyses verify that strain fringes from the Oquirrh Formation in the Grouse Creek Mountains contain phlogopite whereas matrix micas are muscovite, and that in the Black Pine Mountains samples, muscovite is contained within the strain fringes of the deformed sill and within the metasiltite of the contact aureole. From the eight polished sections from the Grouse Creek samples, 4 were selected for the UV laser (F, G, H, and I), and 5 for the $CO_2$ laser (A, B, C, D, and E). From the nine polished sections of the Black Pine samples, 6 were selected for analysis by $CO_2$ laser.

[16] For $^{40}Ar/^{39}Ar$ dating samples were stacked in a Pyrex tube with Fish Canyon Tuff (FCT) sanidine, using an age of 27.9 Ma [*Steven et al.*, 1967; *Cebula et al.*, 1986], as a fluence monitor. Synthetic K-glass and optical grade $CaF_2$ were included to monitor neutron induced argon interferences from K and Ca. Samples were irradiated for 14 h at the Nuclear Science Center at Texas A&M University. Irradiated FCT sanidines together with $CaF_2$ and K-glass fragments were placed in a Cu sample tray in a high vacuum extraction line and were fused using a 20 W $CO_2$ laser. The samples analyzed by the furnace step heating method utilized a double vacuum resistance furnace. Argon isotopic compositions were analyzed using a MAP-215 mass spectrometer at the Nevada Isotope Geochronology Laboratory (NIGL) at UNLV. Mass spectrometer discrimi-
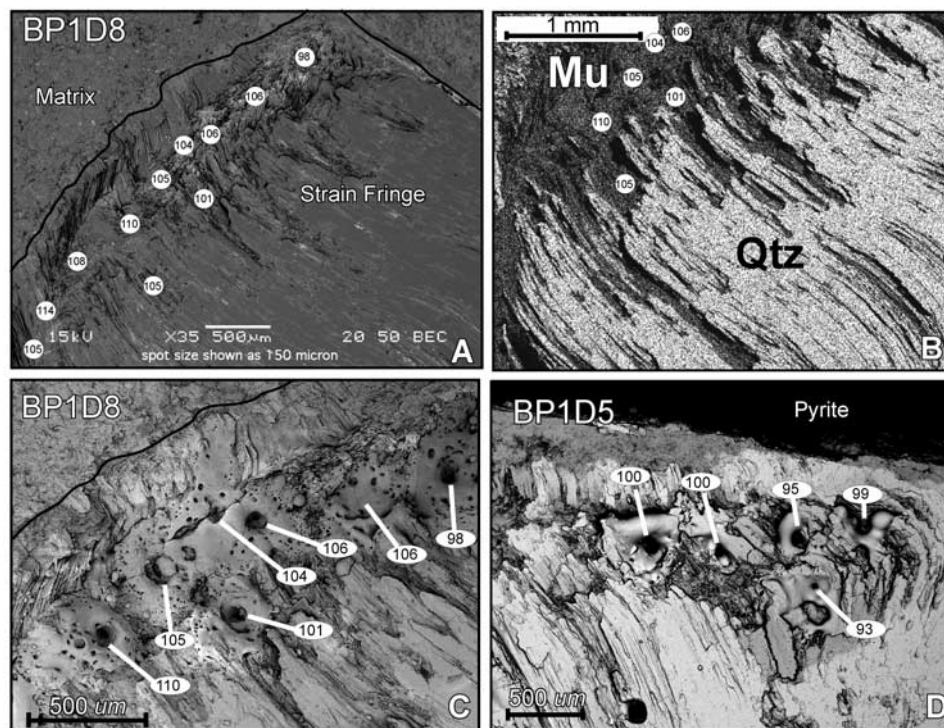
**Figure 5.** Images of quartz-muscovite strain fringes from Black Pine Mountains. (a) SEM BSE image of distal portion of strain fringe BP1D8 prior to laser-probe analyses, showing distribution of ages. (b) Silicon map showing fine-scale intergrown nature of quartz (Qtz, light) and muscovite (Mu, dark), and muscovite rich distal fringe margin near contact with matrix (upper left). Repetition of ages shown for comparison with Figure 5a. (c, d) SEM BSE images of portions of fringes BP1D8 and BP1D5, respectively, showing $CO_2$ laser pits and surrounding and variable accumulations of melt.

nation and sensitivity was monitored by repeated analysis of atmospheric argon aliquots from an online pipette system. Discrimination corrections as well as K and Ca correction factors are given in the appropriate data tables for each sample.

[17] For the Grouse Creek strain fringes, argon was extracted from phlogopite fibers ~100 to 450 $\mu$m wide and up to ~800 $\mu$m in length using two laser systems during two analytical sessions, to be referred to as session one and session two. During session one, we analyzed polished sections from sample 1 and during session two, we analyzed sections from sample 2 and also performed duplicate analyses from sample 1 (Figure 2 and Table 1). During session one, a pulsed 266 nm wavelength Nd-YAG ultraviolet laser focused to a ~10 $\mu$m spot and operated at 4 mJ/pulse and 10–20 Hz was used to extract gas from trenches excavated by rastering the beam over areas of strain fringe surfaces for total gas extraction times of 6–15 min. Rastered areas were ~50,000 to 98,000 $\mu$m$^2$, and were ~5–10 $\mu$m deep. During session one, blanks were acceptably low relative to sample gas yields using the UV laser. During session two, blank levels were significantly higher (see below). Thus, following 4 initial UV analyses of sample 2 (referred to as "duplicate UV analyses"), a second laser system was used. A continuous 10.62 $\mu$m wavelength

$CO_2$ laser focused to a ~100 $\mu$m spot and operated at 1.5–3.0 Watts with 6–10 ms pulses allowed higher sample/blank gas yields by excavating a larger volume of material in a shorter period of time (total gas extraction times of 2–6 min). Control of power levels and pulse lengths was accomplished using custom LabView software. Additionally, three analyses (referred to as "duplicate $CO_2$ analyses") of sections G and F of sample 2, previously analyzed by UV laser, were also conducted using the $CO_2$ laser system. For both laser systems narrower fibers were trenched along their entire length for single analysis, whereas wider fibers were analyzed in two or three growth segments.

[18] Muscovite from the Black Pine strain fringes was analyzed exclusively by the $CO_2$ laser described above, with the exception that total gas extraction times were further reduced to 1 min. Owing to the large size of the muscovite in Black Pine strain fringes, individual analyses were derived from single laser spots of ~100 $\mu$m diameter.

[19] Laser extraction line blanks were measured after every 3–4 analyses (i.e., approximately hourly). Blanks were slightly more variable during session one, thus blank corrections were adjusted to the time of individual analyses by linear interpolation for UV laser analyses. Blanks were more consistent during session two and during analysis of Black Pine strain fringes. Accordingly, average daily blank

**Table 1.** Phlogopite Laser Probe $^{40}$Ar/$^{39}$Ar Data Summary, Grouse Creek Mountains[a]

| Fringe | Age, Ma | 1$\sigma$ | %$^{40}$Ar* | Mean Ages > 65% $^{40}$Ar* |
|--------|---------|-----------|-------------|----------------------------|
| *Sample 1, UV Analyses* | | | | |
| F | 105.09 | 1.51 | 73.9 | All (n = 15) |
| F | 100.18 | 1.17 | 73.2 | Mean = 105.0 ± 5.8 Ma |
| F | 101.70 | 0.70 | 72.2 | |
| F | 97.45 | 0.59 | 70.2 | F (n = 4) |
| F | 95.38 | 0.57 | 64.9 | Mean = 101.1 ± 3.2 Ma |
| F | 94.11 | 1.05 | 56.7 | |
| *F* | *90.88* | *0.78* | *57.6* | |
| G | 104.14 | 2.20 | 83.3 | |
| G1 | 108.76 | 0.97 | 78.2 | |
| G1 | 106.34 | 1.66 | 78.1 | |
| G1 | 111.10 | 1.66 | 76.1 | |
| G1 | 102.52 | 1.53 | 73.4 | G (n = 9) |
| G3 | 107.73 | 1.45 | 70.3 | Mean = 106.6 ± 2.5 Ma |
| G1 | 107.05 | 2.10 | 69.6 | |
| G4 | 106.99 | 0.82 | 67.3 | |
| G1 | 92.13 | 2.32 | 55.7 | |
| G1 | 93.47 | 2.27 | 53.3 | |
| *G1* | *105.16* | *0.72* | *66.5* | |
| *G1* | *96.63* | *1.08* | *54.8* | |
| H | 109.66 | 0.75 | 76.9 | H (n = 1,109.7 ± 0.8 Ma) |
| I | 101.23 | 1.13 | 66.8 | I (n = 1,101.2 ± 1.1 Ma) |
| *Sample 2, CO$_2$ Analyses* | | | | |
| A | 97.19 | 1.55 | 90.5 | All (n = 12) |
| A | 98.62 | 0.62 | 88.1 | Mean = 92.5 ± 5.0 |
| A | 90.87 | 1.27 | 85.9 | |
| A | 83.85 | 2.37 | 77.1 | |
| A | 94.58 | 1.01 | 74.8 | |
| A | 93.57 | 2.00 | 71.2 | A (n = 9) |
| A | 75.96 | 5.58 | 52.4 | Mean = 92.3 ± 5.1 Ma |
| *A* | *94.99* | *4.94* | *89.7* | |
| *A* | *84.87* | *0.95* | *74.7* | |
| *A* | *92.36* | *3.24* | *66.8* | |
| *A* | *77.12* | *2.93* | *63.8* | |
| B | 95.16 | 1.71 | 85.8 | |
| B | 86.66 | 2.31 | 82.7 | B (n = 3) |
| B | 97.37 | 7.63 | 73.1 | Mean = 93.1 ± 5.6 Ma |
| B | 71.10 | 1.90 | 62.8 | |
| B | 100.88 | 10.86 | 61.9 | |
| C | 85.08 | 1.35 | 57.7 | |
| C | 81.94 | 2.16 | 51.5 | C (none) |
| C | 80.70 | 1.07 | 38.3 | |
| D | 78.84 | 4.14 | 58.1 | |
| D | 91.09 | 2.66 | 55.6 | D (none) |
| D | 74.63 | 4.62 | 43.2 | |
| D | 78.34 | 5.13 | 40.5 | |
| *D* | *66.81* | *1.58* | *26.0* | |
| E | 82.48 | 3.31 | 62.8 | |
| E | 83.43 | 1.48 | 60.6 | E (none) |
| E | 77.67 | 5.26 | 51.0 | |
| E | 62.18 | 5.02 | 37.0 | |

[a]Italics denote the following: Sample 1, CO$_2$ analyses; Sample 2, UV analyses.

values were used for CO$_2$ laser analyses. Data reduction using different blank correction schemes did not result in significant changes in variability of calculated ages or in mean ages for individual strain fringes. Laser-probe sample gas yields resulted in blank $^{40}$Ar corrections ranging from 13 to 34% of the measured $^{40}$Ar for UV analyses and from 0.6% to 17.1% for CO$_2$ analyses during analysis of Grouse Creek samples in sessions one and two. Blank $^{40}$Ar correc-

tions were significantly lower at 0.1% to 1.9% for CO$_2$ analyses of Black Pine samples. Average blank values for all argon isotopes during laser-probe analyses are given in auxiliary material Data sets S1, S2, and  S4[1]. Furnace blanks measured prior to step heating analyses averaged 0.04 mV for $^{36}$Ar and 5.76 mV for $^{40}$Ar at temperatures <1200°C, and 0.07 mV for $^{36}$Ar and 9.48 mV for $^{40}$Ar at temperatures >1200°C. Furnace blanks for all other argon isotopes were <0.02 mV.

## 6.  The $^{40}$Ar/$^{39}$Ar Data Treatment and Results

[20]  Laser-probe data is summarized in Tables 1 and 2; the full data sets are given in auxiliary material Data sets S1, S2, and  S4. All uncertainties are reported at the 1$\sigma$ level.

### 6.1.  Grouse Creek Strain Fringes

[21]  For sample 1, 18 apparent ages by UV laser probe vary from 92.1 Ma to 111.1 Ma (average 102.5 ± 5.8 Ma) (Figures 6 and 7 and  Table 1) whereas 3 apparent ages by CO$_2$ laser probe ("duplicate" CO$_2$ analyses) vary over a similar range from 90.9 to 105.2 Ma (Table 1 and Data Set S1). For sample 2, 23 apparent ages by CO$_2$ laser probe vary from 62.2 Ma to 100.9 Ma (average 85.3 ± 9.7 Ma), whereas 5 UV laser-probe analyses ("duplicate" UV analyses) also vary over a similar range from 66.8 to 95.0 Ma (Figures 6 and 7, Table 1, and Data Set S2).

[22]  Owing to concerns about degassing adjacent minerals in the strain fringe (quartz and calcite) with the CO$_2$ laser, several analyses of these phases were performed. None yielded measurable $^{40}$Ar above atmospheric values, thus indicating that no degassing of adjacent mica occurred and that there was no contribution of excess argon from fluid inclusions. For example, an analysis of quartz from Grouse Creek sample D yielded argon concentrations within uncertainty of blanks except for $^{36}$Ar and $^{40}$Ar, which were slightly above blank levels and yielded a $^{40}$Ar/$^{36}$Ar ratio (290.8 ± 12.1) within uncertainty of the atmospheric value (i.e., no detectable radiogenic or excess argon). Problems with degassing of adjacent minerals during CO$_2$ laser analysis of micas can potentially be further addressed via measured $^{37}$Ar and $^{38}$Ar, as $^{37}$Ar is derived from Ca (adjacent calcite) and $^{38}$Ar is derived from Cl (excess argon may be associated with Cl-enriched fluid inclusions in quartz). As Cl-derived $^{38}$Ar is produced via a thermal neutron interaction during irradiation we were unable to use this tracer owing to the boron nitride shielding used at the Texas A&M reactor. However, we note that there is no significant difference in Ca/K values (calculated from measured $^{37}$Ar/$^{39}$Ar ratios) from UV and CO$_2$ laser analyses from Grouse Creek sample 1 (Data Set S1). Similarly, with the exception of three analyses there is no significant difference in Ca/K from UV and CO$_2$ laser analyses from Grouse Creek sample 2 (Data Set S2). Three CO$_2$ analyses have Ca/K > 1 and may reflect degassing of adjacent calcite. The ages calculated for two of these analyses are similar to

[1]Auxiliary materials are available at ftp://ftp.agu.org/apend/tc/ 2007tc002153.

**Table 2.** Muscovite $CO_2$ Laser Probe $^{40}Ar/^{39}Ar$ Data Summary, Black Pine Mountains

| Fringe | Age, Ma | $1\sigma$ | Location[a] | Mean Ages |
|--------|---------|-----------|-------------|-----------|
| D1 | 97.23 | 0.81 | P | All (n = 44) |
| D1 | 96.84 | 0.83 | P | Mean = 104.66 ± 5.82Ma |
| D1 | 101.16 | 0.94 | P | |
| D1 | 107.90 | 3.36 | P | |
| D1 | 108.14 | 1.15 | P | All D1 (n = 12) |
| D1 | 108.50 | 0.89 | P | 105.48 ± 4.33 Ma |
| D1 | 106.21 | 0.97 | P | |
| D1 | 106.29 | 0.83 | P | |
| D1 | 106.28 | 3.77 | P | |
| D1 | 108.38 | 0.81 | D | |
| D1 | 108.78 | 0.84 | D | |
| D1 | 110.01 | 1.09 | D | |
| D2 | 101.12 | 0.71 | D | All D2 (n = 3) |
| D2 | 108.32 | 0.90 | D | Mean = 107.44 ± 5.92 Ma |
| D2 | 112.87 | 0.97 | D | |
| D4 | 112.65 | 0.88 | D | All D4 (n = 5) |
| D4 | 104.48 | 0.77 | D | Mean = 112.49 ± 4.30 Ma |
| D4 | 113.39 | 0.90 | D | |
| D4 | 114.68 | 0.93 | D | |
| D4 | 117.25 | 1.20 | D | |
| D5 | 100.08 | 0.76 | P | All D5 (n = 6) |
| D5 | 99.59 | 2.20 | P | Mean = 97.44 ± 2.66 Ma |
| D5 | 95.40 | 1.36 | P | |
| D5 | 98.98 | 1.76 | P | |
| D5 | 92.54 | 0.90 | P | |
| D5 | 98.03 | 1.18 | P | |
| D6 | 96.01 | 0.85 | P | All D6 (n = 4) |
| D6 | 98.70 | 0.78 | P | Mean = 98.56 ± 1.82 Ma |
| D6 | 101.16 | 0.96 | P | |
| D6 | 98.39 | 0.92 | P | |
| D8 | 105.11 | 0.82 | D | All D8 (n = 14) |
| D8 | 105.76 | 0.74 | D | Mean = 105.42 ± 4.16 Ma |
| D8 | 110.39 | 0.85 | D | |
| D8 | 105.48 | 0.88 | D | |
| D8 | 104.08 | 0.78 | D | |
| D8 | 108.04 | 0.74 | D | |
| D8 | 98.25 | 0.78 | D | |
| D8 | 100.69 | 0.82 | D | |
| D8 | 104.98 | 0.87 | D | |
| D8 | 104.66 | 0.82 | D | |
| D8 | 114.35 | 0.95 | D | |
| D8 | 104.89 | 0.71 | P | |
| D8 | 109.71 | 0.94 | P | |
| D8 | 99.48 | 0.79 | P | |

[a]P, proximal; D, distal.

other ages from this sample, whereas the third is the youngest of the $CO_2$ analyses (62.1 Ma) and has the lowest radiogenic yield (37% $^{40}Ar*$). These results suggest that in general the ages calculated from $CO_2$ laser analyses do not reflect significant contributions from degassing of adjacent mineral phases in the strain fringes.

[23] There are distinct correlations between age and radiogenic yield as well as between ages and individual strain fringes. For both data sets apparent age is positively correlated with radiogenic yield (Figure 6), although the correlation is more pronounced for the data from sample 2, which exhibits lower ages and a wider range of radiogenic yields. As discussed further below, we interpret the lowered radiogenic yields and apparent ages to be principally the result of localized alteration/deformation and resulting

argon loss, with some potential degassing of adjacent low-K phases in the case of the $CO_2$ laser. We suggest that sample 2, closer to the Middle detachment fault than sample 1 (15 versus 150 m), was affected by a greater degree of postgrowth intracrystalline strain and/or fluid interaction relative to sample 1. Accordingly, both data sets were filtered to exclude low radiogenic yield–young age outliers by focusing on analyses with %$^{40}Ar* > 65$ (Figures 6 and 7 and Table 1) on the basis of the assumption that higher radiogenic yield analyses are less affected by alteration, deformation or potential degassing of adjacent low-K phases.

[24] For laser-probe data from sample 1, 15 of 18 analyses have radiogenic yields >65% (Figures 5 and 6 and Table 1) and define a mean age of 105.0 ± 5.8 Ma (Figure 6). A single analysis of fringe H produced an age of 109.7 ± 0.8 Ma and a single analysis of fringe I produced and age of 101.1 ± 3.2 Ma. Four analyses from F yielded a mean age of 101.1 ± 2.8 Ma, whereas 9 analyses from G gave a mean age of 106.6 ± 2.5 Ma (Table 1).

[25] For laser-probe data of sample 2, 12 of 28 individual analyses have radiogenic yields > 65% (Figure 6 and 7 and Table 1). These 12 analyses define a mean age of 92.5 ± 5.0 Ma (Figure 7). Strain fringes A and B account for all 12 of these analyses; there were no analyses with radiogenic yields >65% from C, D and E. Nine analyses from strain fringe A define a population with a mean age of 92.3 ± 5.1 Ma, whereas 3 analyses from B define an indistinguishable mean age of 93.1 ± 5.6 Ma. These ages from sample 2 are generally younger than those obtained from sample 1, although mean ages all overlap at the $2\sigma$ uncertainty level.

[26] The $CO_2$ laser-probe data from sample 2 show the greatest variability in radiogenic yield and calculated Ca/K ratios, the widest range of ages, lower average radiogenic yield and a younger average age than UV data from sample 1 (Figures 6 and 7 and Table 1). Data from individual strain fringes exhibit similar relationships. Meaningful inverse isochrons [*Wendt and Carl*, 1991] for sample 2 were not obtained. However, 7 of 12 analyses from strain fringe G of sample 1 (Table 1) define a statistically valid isochron with an age of 102.2 ± 2.1 Ma and a $^{40}Ar/^{36}Ar$ intercept of 314 ± 18 (Figure 8). Note that this isochron age is in agreement with both the mean age of the analyses from fringe G as well as the mean age of all analyses of sample 1.

[27] Detrital muscovite separated from the matrix of both samples 1 and 2 was step-heated to aid in the interpretation of the age significance of the phlogopite laser-probe ages. The muscovite from sample 1 yields a discordant stair-stepped age spectrum with an initial age of 97 Ma, rising to 416 Ma (Figure 9), and a total gas age of 319.9 ± 1.4 Ma (Data Set S3). Sample 2 matrix muscovite yields an age spectra of similar morphology, but with lower ages overall at comparable $^{39}Ar$ gas release to the age spectra from sample 1 (Figure 9). The muscovite from sample 2 yields a discordant stair-stepped age spectrum with an initial age of 69 Ma, rising to 358 Ma (excluding the final 0.6% gas release, Figure 9), and a total gas age of 251.85 ± 0.94 Ma (Data Set S3). For both muscovites, aside from the first ~10–15% of the gas released, Ca/K ratios are consistent,
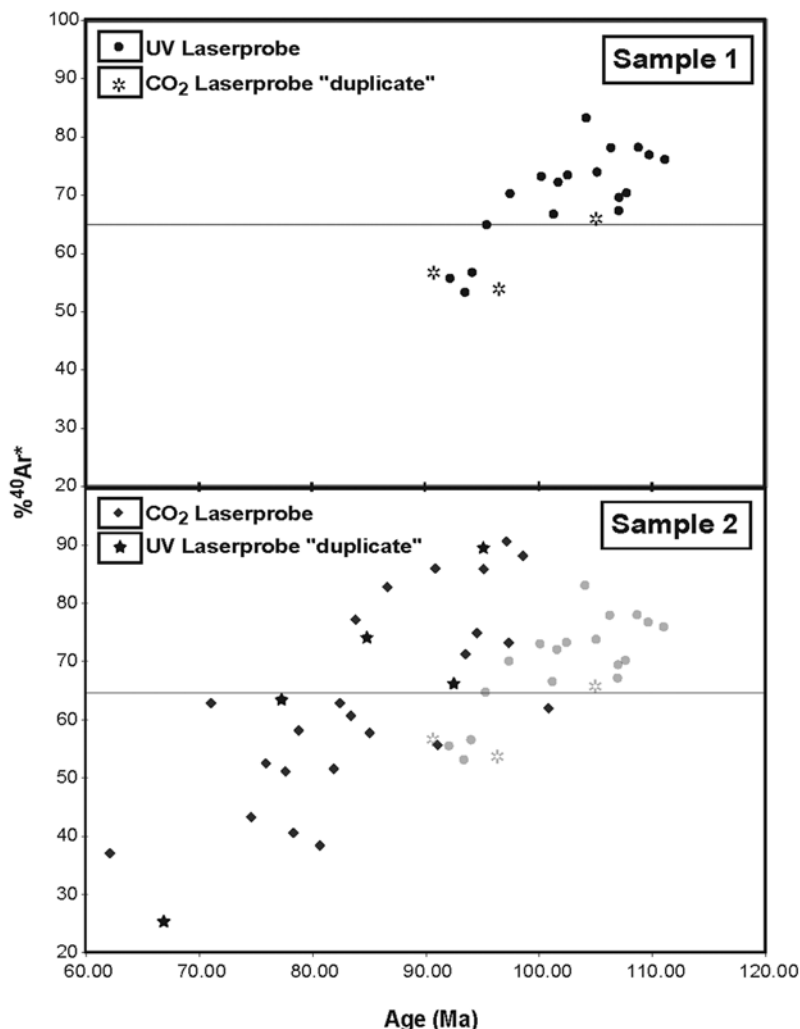
**Figure 6.** Plots of age (Ma) versus radiogenic yield (% $^{40}$Ar*) for $CO_2$ and UV laser-probe analyses. Symbols are noted on diagram. Horizontal line separates analyses with radiogenic yield >65% from those with lower yield. Symbols in gray in bottom plot are analyses of sample 1, for comparison. Note distinct positive correlation between age and % $^{40}$Ar*.

suggesting that outgassing of a single homogeneous mineral dominates the gas released from the samples (Data Set S3). The higher Ca/K in the initial gas released may indicate minor recrystallization, neocrystallization or minor amounts of a secondary mineral within the mica.

### 6.2. Black Pine Strain Fringes

[28] The 44 $CO_2$ laser-probe analyses of muscovite from 6 strain fringes yield apparent ages varying from 92.54 ± 0.90 Ma to 117.25 ± 1.20 Ma (average 104.66 ± 5.82 Ma) (Figure 10, Table 2, and Data Set S4). Mean ages for the 6 strain fringes are 105.48 ± 4.33 Ma (D1, n = 12), 107.44 ± 4.84 (D2, n = 3), 112.49 ± 4.3 Ma (D4, n = 5), 97.44 ± 2.66 Ma (D5, n = 6), 98.56 ± 1.82 Ma (D6, n = 4), and 105.42 ± 4.16 Ma (D8, n = 14). Unlike the Grouse Creek phlogopite analyses, the Black Pine muscovite analyses do not show a correlation between radiogenic yield and apparent

age, although 2 of the 5 analyses with radiogenic yields <50% are the oldest of the 44 apparent ages and are thus suspect. We note, however, that there is little variation (<1 Ma) in the mean ages of the analyses when the cutoffs of >50%, >60%, and >70% radiogenic yield are applied.

[29] There is an apparent relationship between the position within the strain fringe and age (Figure 10). The majority of analyses from the strain fringes are either near the matrix (distal fringe) or near the pyrite (proximal fringe). The mean ages of analyses from the distal parts of the analyzed fringes are all older than the mean age of analyses from the proximal parts of the fringes (Table 2). However, because ages from the proximal parts of the strain fringes overlap with ages from the distal parts of the strain fringes within uncertainties (Figure 10 and Table 2) we are hesitant to attribute the differences in the mean ages to progressive growth of the strain fringe. Rather, owing to the proximity
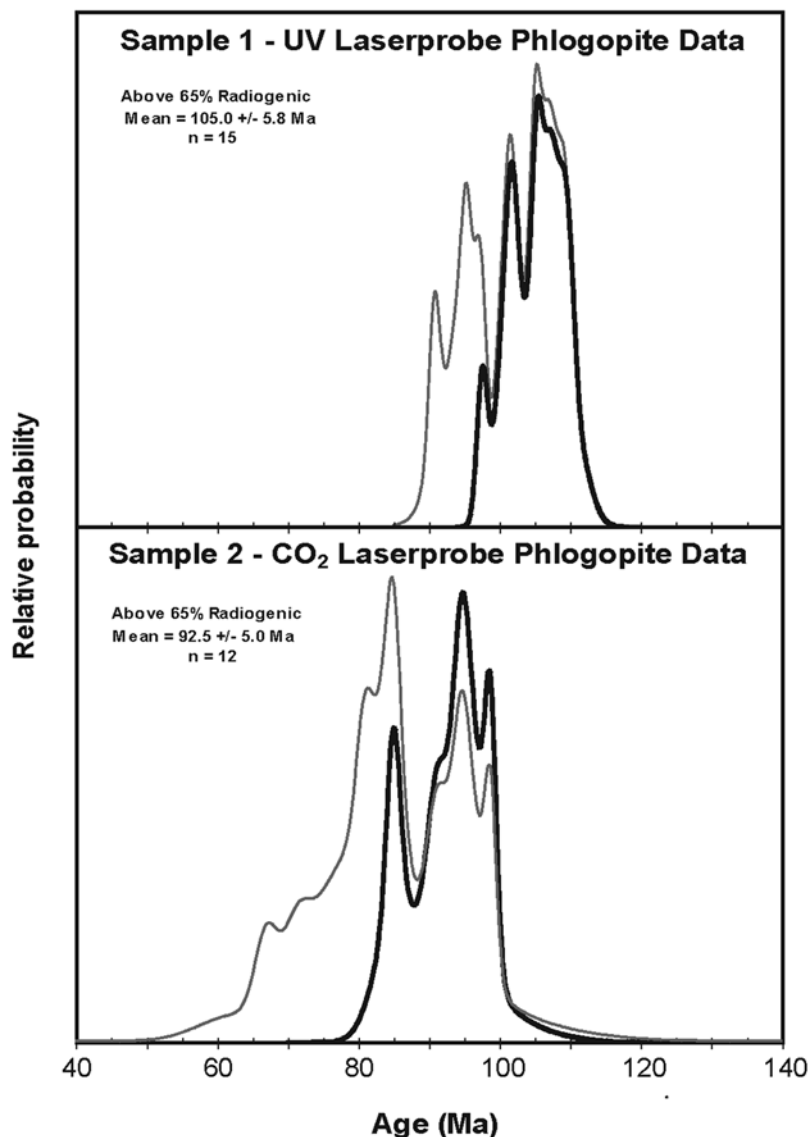
**Figure 7.** Probability distribution plots for $CO_2$ and UV laser probe analyses of phlogopite from strain fringes in the Oquirrh Formation. Bold black line represents analyses with $^{40}Ar^* > 65\%$ as shown in Figure 6. Thin gray line represents all analyses.

of the younger age spots to the relict pyrite (now goethite), and owing to the necessity of hydrothermal alteration of the pyrite in formation of goethite, we consider that the young ages may be related to slight post-fringe-growth argon loss.

[30] A previously reported step-heated muscovite separate from the contact aureole of the pyrite-bearing sill yielded a plateau age of 144.3 ± 0.75 Ma [*Wells et al.*, 1990]. A new step-heated muscovite separate of a second sample of contact-metamorphosed Manning Canyon Shale yielded an indistinguishable plateau age of 144.0 ± 0.77 Ma (Figure 11 and Data Set S5). Following *Wells et al.* [1990], these ages are interpreted to date the intrusion, and because the intrusion is cleaved, provide a lower age limit for cleavage formation. Furthermore, these ages aid in the

interpretation of the age significance of the muscovite laser-probe ages.

## 7. Discussion

### 7.1. The $^{40}Ar/^{39}Ar$ Age Constraints

[31] The question arises as to whether the differences in ages between samples 1 and 2 from the Grouse Creek Mountains are a result of the primary method of analysis (the UV versus $CO_2$ laser probe) or unanticipated inherent differences between samples collected at different structural levels above the Middle detachment fault. The duplicate UV and $CO_2$ analyses (Table 1 and Figure 6), while few, provide some constraints on this question. While the average age of
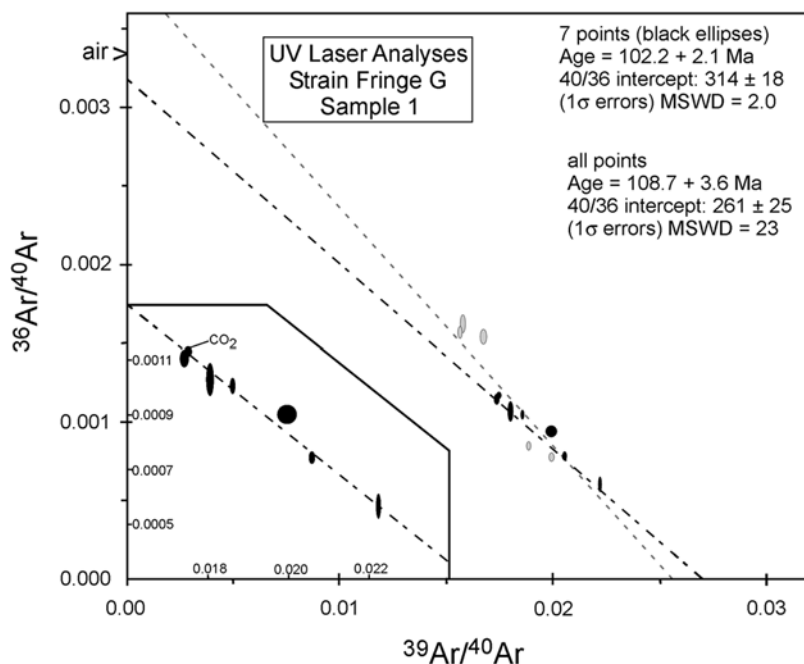
**Figure 8.** Isochron plot for phlogopite analyses from strain fringe G, sample 1. All data points are UV analyses unless marked $CO_2$. Uncertainties are at $1\sigma$; error ellipses shown at $2\sigma$. Inset shows the seven points that define the statistically valid isochron.

the UV analyses of sample 1 is older than the average age of the $CO_2$ analyses of sample 2 (Figure 7), the average age of the duplicate $CO_2$ analyses of sample 1 is older than the average age of the duplicate UV analyses of sample 2 (Table 1 and Data Sets S1 and S2); that is, age is more strongly correlated with sample than with the applied laser technique. This difference can be appreciated by inspection of Figure 6, which shows that the duplicate analyses show a greater affinity with the sample than with the technique. Thus, we interpret the differences in age populations between samples 1 and 2 to be a result of differences in the present radiogenic argon concentration (or concentration gradient) in phlogopite between samples rather than an artifact of the laser ablation technique.

[32] Determining the cause of the age differences between samples 1 and 2 (Figures 6 and 7) and which ages carry geologic significance should be possible if we understand the cause of the association between apparent age and radiogenic argon for the phlogopite analyses (Figure 6). The presence of excess argon ($^{40}Ar_E$) appears unlikely as an explanation for several reasons. If $^{40}Ar_E$ were distributed homogeneously throughout phlogopites within the strain fringes, then calculated apparent ages (Table 1 and Data Sets S1 and S2) should exhibit an inverse correlation between age and radiogenic yield, which is opposite of what is seen. Low radiogenic yield analyses, as compared to higher radiogenic yield analyses, would have corresponding larger under corrections for nonradiogenic argon resulting in greater apparent ages. This is often seen in step heating data yielding U-shaped age spectra that have low radiogenic yields in the early and late steps with anomalously old ages, and higher radiogenic yields in the middle gas release that

approach the true age of the sample. The incorporation of $^{40}Ar_E$ in fluid inclusions would yield less predictable results for laser-probe data. In addition, Ordovician rocks of higher metamorphic grade ($\sim500°C$) below the Middle detachment that bear $D_1$ fabrics have yielded $88-90$ Ma muscovite $^{40}Ar/^{39}Ar$ cooling ages [Wells et al., 1990, 1998]; this indicates that $D_1$ phlogopite growth in the Oquirrh Formation
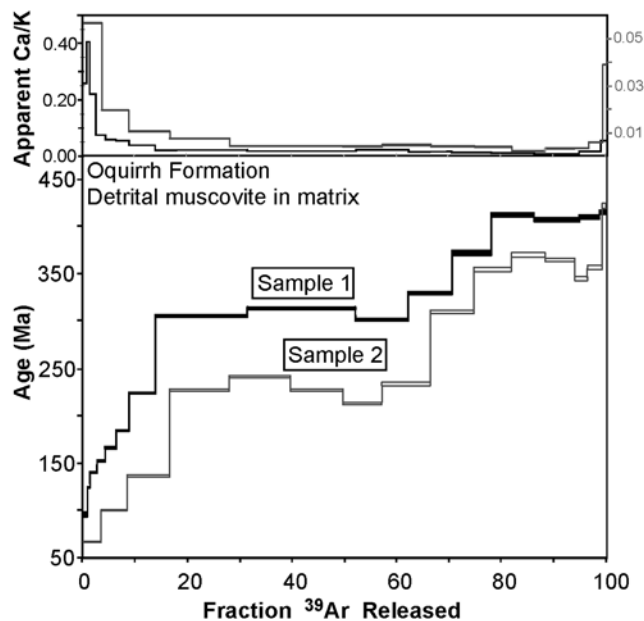


**Figure 9.** Ca/K plots and age spectra for matrix (detrital) muscovite from samples 1 and 2.
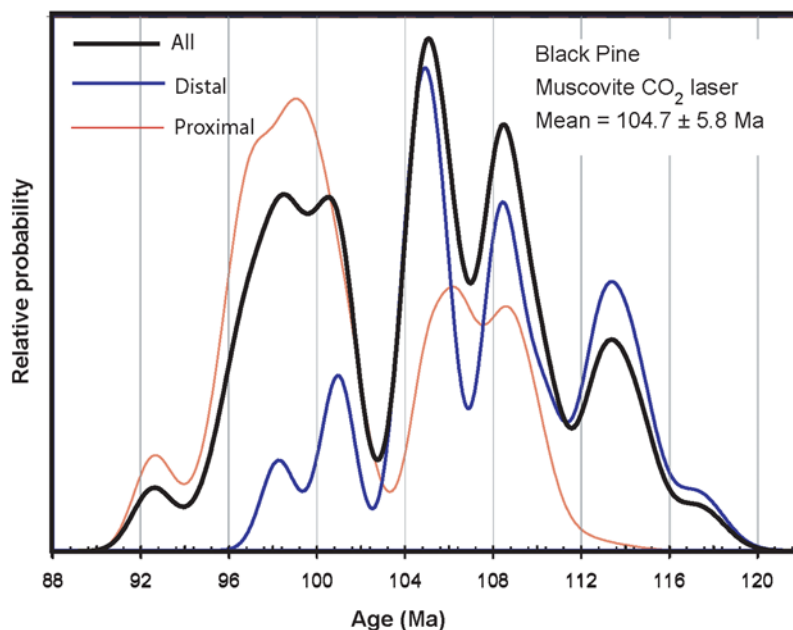
**Figure 10.** Probability distribution plots for $CO_2$ laser probe analyses of muscovite from strain fringes from Black Pine Mountains. Bold line represents all analyses; intermediate width line represents analyses from distal end of fringes; and thin line represents analyses from proximal end of fringes.

must be older than 90 Ma, and further indicates that variable incorporation of excess argon is an unlikely explanation for the observed range of apparent ages of phlogopite. Furthermore, post-mineral-growth effects of fluids related to the Middle detachment fault would be expected to contribute atmospheric argon, not excess argon, as fluids in and near detachment faults have been shown to be dominantly meteoric [e.g., *Morrison and Anderson*, 1998; *Mulch et al.*, 2005].

[33] Consistent differences between the UV and $CO_2$ laser data sets (lower radiogenic yields and correlated younger ages for the $CO_2$ data) suggests that the age-radiogenic yield correlation (Figure 6) may in part be controlled by outgassing of adjacent low-K minerals (quartz and calcite). In addition, petrographic observations indicate discrete zones of chlorite intergrowth and deformation features such as kink bands. Clearly, the larger $CO_2$ beam diameter (~100 $\mu$m versus ~10 $\mu$m for the UV laser), along with the significant thermal halo produced around $CO_2$ melt pits, is more likely to sample such areas of potential argon loss and also to degas adjacent quartz and calcite. Ca/K values for $CO_2$ analyses of sample 2 are more variable than those for UV analyses of sample 1. However, as previously discussed, Ca/K values for $CO_2$ laser and UV laser analyses are, with few exceptions, similar for analyses of the same sample (Data Sets S1 and S2). Recoil redistribution of $^{39}Ar$ (or $^{37}Ar$) between intergrown phases such as chlorite and phlogopite and calcite and phlogopite would likely produce highly variable $^{37}Ar/^{39}Ar$ and associated variability in ages between analyses which sample significant volumes of chlorite/calcite relative to phlogopite. However, there is no correlation between age and Ca/K ($^{37}Ar/^{39}Ar$) apparent in the data sets for either the UV or the $CO_2$ analyses. These observations indicate that degassing of adjacent mineral phases is not significant for either laser system, and that

the larger spot size and thermal halo of the $CO_2$ laser does not contribute to larger degrees of outgassing of adjacent minerals or altered/deformed areas.

[34] Laser-probe argon ages such as those presented here may be sensitive to inaccurate blank measurements. In particular, relatively small inaccuracy in blank $^{36}Ar$ measurements could potentially produce significant variability in
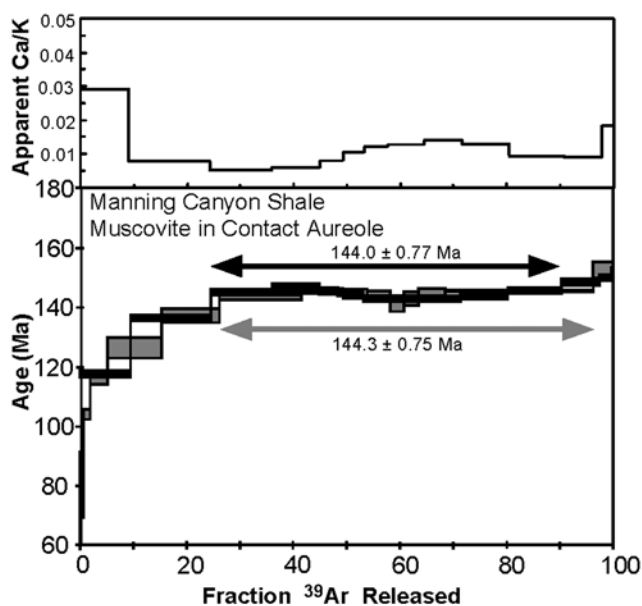


**Figure 11.** The $^{40}Ar/^{39}Ar$ age spectra of muscovite from Manning Canyon Shale within contact aureole of intermediate sill. Grey, previous analysis reported by *Wells et al.* [1990]; black, new analysis.

atmospheric $^{40}$Ar corrections, and thus calculated ages and radiogenic yields. Multiple data reduction approaches were assessed, including utilizing blanks measured prior to analysis, using previous and subsequent blank averages, interpolating blank values to the time of sample analysis and using daily blank averages. These data reduction schemes resulted in insignificant changes in calculated ages, and mean ages, relative to analytical uncertainties. For example, ages calculated for UV analyses of strain fringe G in sample one using blanks measured prior to analyses resulted in a mean age of 105.7 ± 2.4 Ma (n = 8), as compared to 106.6 ± 2.5 Ma (Table 1) using time interpolated blanks. Ages calculated for $CO_2$ analyses of strain fringe B in sample two using blanks measured prior to analyses resulted in a mean age of 94.3 ± 5.5 Ma (n = 3), as compared to 93.1 ± 5.6 Ma (Table 1) using averaged daily blanks. There is no correlation between the magnitudes of the blank $^{36}$Ar correction and the calculated ages and radiogenic yields, as might be expected if inaccurate $^{36}$Ar blanks were causing overcorrection or undercorrection for atmospheric argon. Finally, $CO_2$ data from the Black Pine samples (Table 2 and Data Set S4), which do not show age/radiogenic yield correlations and have significantly lower blank corrections, yield a similar average age (∼105 Ma) to >65% radiogenic yield Grouse Creek sample 1 analyses.

[35] We suggest that the unanticipated differences in ages between samples 1 and 2 (Figures 6 and 7) and the correlation between apparent age and radiogenic argon (Figure 6) are most consistent with variable argon loss, most likely resulting from fluid-induced alteration combined with intragrain deformation. The significantly lower ages recorded for matrix muscovite in sample 2 as compared to sample 1 is consistent with this interpretation. Unfortunately, we are not able to chemically map the analyzed grains because, during analysis by $CO_2$ laser, the material has been consumed. However, petrographic observations from other strain fringes from samples 1 and 2 that have implications for the age-radiogenic argon correlation include volumetrically minor, but perhaps significant, zones of chlorite intergrowth. Argon loss related to intragrain recrystallization, deformation and defects has been both modeled [Reddy et al., 1996] and documented [Reddy et al., 1996; Mulch et al., 2002] in numerous studies. Additionally, altered, and even incipiently altered, biotite has been shown to undergo argon loss [Roberts et al., 2001], leading to correlations between age and radiogenic argon. Similarly, a correlation between age and radiogenic argon has been noted from variably chloritized biotite [Di Vincenzo et al., 2004]. These examples of correlations between age and radiogenic argon provide a basis for interpretation of the similar correlations determined in this study of phlogopite. Roberts et al. [2001] and Di Vincenzo et al. [2004] suggest that analyses with lower $^{36}$Ar/$^{39}$Ar or lower atmospheric argon (i.e., higher radiogenic yield) are most reliable, consistent with our interpretation of the laser-probe $^{40}$Ar/$^{39}$Ar results from phlogopite.

[36] The interpretation that phlogopite ages record timing of growth below the $T_c$, as discussed below, also has implications for measured age variability. Crystallization

above the $T_c$ and subsequent slow cooling would result in age gradients perpendicular to the $c$ axis. Laser-probe analyses sampling variable depths in this plane would be expected to yield variable ages if the age gradient were sufficiently pronounced. Since phlogopite apparently crystallized below it's $T_c$ such age gradients should not be present, and thus measured variability in ages cannot be attributed to intracrystalline gradients in $^{40}$Ar*. This is substantiated by the lack of correlation between age and width of the analyzed phlogopite fibers.

[37] Previous efforts to date strain fringes using Rb-Sr dating of microdrilled samples have shown that in some cases, a significant variation in ages may result from progressive growth of the strain fringe [Müller et al., 2000]. The UV and $CO_2$ data presented here show no systematic age differences between the inner and outer portions of the fibrous strain fringes. This probably reflects the relative accuracy and precision of the method for low argon yields and also complications with nonsystematic alteration and argon loss, rather than either uncertainty in the growth model or an indication of strain rates.

[38] In summary, the laser-probe analyses from sample 1, regardless of the use of UV or $CO_2$ laser, are older overall than those from sample 2 (Figures 6 and 7 and Table 1); these differences are interpreted to indicate differences in the postgrowth alteration and deformation of phlogopite at these different structural levels in otherwise compositionally similar rocks. The analyses from sample 2, most of which were determined by $CO_2$ laser probe, are considered to be less reliable. The laser-probe $^{40}$Ar/$^{39}$Ar data from sample 1 (of >65% radiogenic yield), consisting of 14 UV and 1 $CO_2$ analyses, define a mean age of 105.0 ± 5.8 Ma, a weighted mean age of 104.2 ± 2.3 Ma, and an isochron age (strain fringe G) of 102.2 ± 2.1 Ma. Thus, our best estimate of the age of strain fringe growth, and thus the timing of $D_1$ deformation, consistent with the available geologic and geochronologic data, is conservatively, 105 ± 6 Ma.

[39] The $CO_2$ laser is not routinely used for in situ work, owing to the larger $CO_2$ beam diameter (∼100 $\mu$m versus ∼10 $\mu$m for the UV laser) and the significant thermal halo produced around $CO_2$ melt pits, leading to potential complications of directly sampling adjacent minerals or of thermally activated diffusion from such minerals. However, the micas analyzed in this study are predominantly encased within quartz and calcite, phases which were analyzed separately and shown to have only atmospheric argon. $CO_2$ laser ablation may have utility for in situ work in cases of armoring of K-bearing phases (e.g., mica inclusion in garnet, strain fringes of this study), particularly in relatively young materials.

## 7.2. Growth or Cooling Ages?

[40] The tectonic significance of the laser-probe strain fringe ages depends upon whether the temperature of deformation and mica growth was above or below the relevant closure temperature ($T_c$). If growth occurred above the $T_c$ then ages represent the timing of subsequent cooling through the $T_c$. If growth occurred below the $T_c$ then ages represent the timing of growth, and thus deformation.
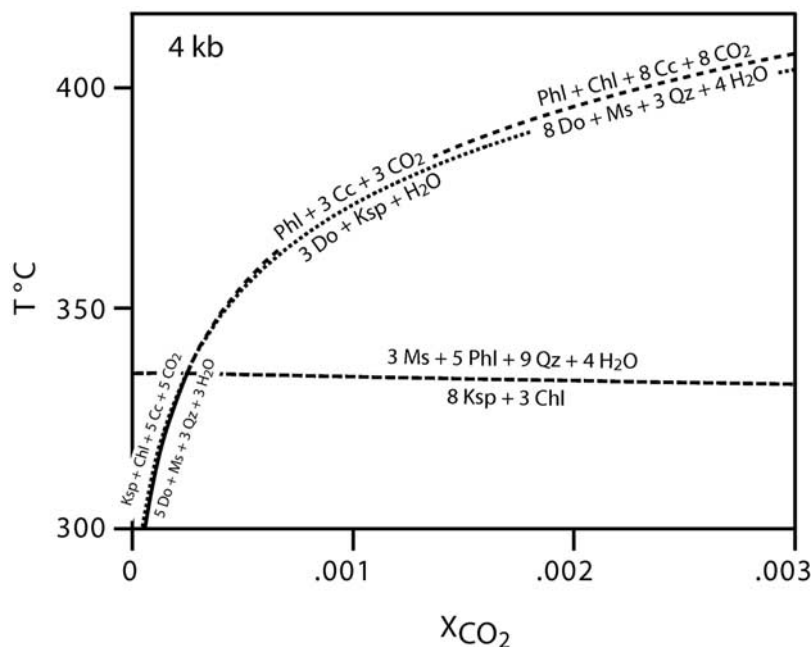
**Figure 12.** Reactions in the system quartz + dolomite + muscovite ($K_2O$-$MgO$-$CaO$-$SiO_2$-$Al_2O_3$-$H_2O$-$CO_2$) at 4 kb, showing the isobaric invariant point that occurs at very $H_2O$-rich conditions and at temperatures consistent with the production of phlogopite below 350°C. Calculated using the data and methods of *Berman* [1988] and assuming fully disordered K-feldspar (adularia, assumed to be thermodynamically equivalent to sanidine). Because the fluid mixing model of *Kerrick and Jacobs* [1981] fails below 330°C at 4 kbar, the lines shown were extrapolated from lines calculated above 330°C. Cc, calcite; Chl, clinochlore; Do, dolomite; Ksp, K-feldspar; Ms, muscovite; Phl, phlogopite; Qz, quartz.

Several lines of evidence indicate that growth occurred below the $T_c$ for phlogopite in the Grouse Creek Mountains and below the $T_c$ for muscovite in the Black Pine Mountains. For the phlogopite from the Grouse Creek Mountains, we focus on sample 1, which yields the most reliable ages, as previously discussed.

[41] Phlogopite growth at 300–350°C is suggested by a variety of observations. Petrographic examination shows that the matrix consists of abundant fine-grained calcite and dolomite and detrital muscovite, quartz, plagioclase, and microcline. The relevant reaction bundle is shown in Figure 12. The strain shadows include phlogopite and calcite but lack muscovite and clinochlore, which is consistent with phlogopite growth by the reaction shown in Figure 12 by the dotted line. Conodont color alteration indices of 5, reported from various exposures of the greenschist-facies Oquirrh Formation in the Raft River–Albion–Grouse Creek metamorphic core complex [*Wells et al.*, 1990, 1997], indicate temperatures of 300–370°C over timescales of 1–10 Ma [*Rejebian et al.*, 1987]. Temperatures of 300–350°C are also consistent with the deformation mechanism of solution-transfer creep (pressure solution) evident in quartz, carbonate minerals and phyllosilicates in the calcareous metasiltstone [*Rutter*, 1983].

[42] The age spectra for the matrix muscovite (Figure 9) are consistent with either partial thermal resetting of detrital muscovite or mixing of detrital and neocrystallized syntectonic muscovite. The small range of Ca/K ratios (Data Set S3) and small percentage of the early age spectra gas release showing slightly elevated values (Figure 9) does not support the presence of significant quantities of neocrystallized muscovite, although minor neocrystallization cannot be ruled out on the bases of this data [c.f. *Di Vincenzo et al.*, 2004; *Wijbrans and McDougall*, 1986]. However, electron microprobe analyses suggest the presence of only one muscovite population in the matrix. Additionally, there is no petrographic evidence for syndeformational muscovite growth in the matrix. These observations thus support a partial thermal resetting interpretation for the matrix muscovite age spectra (Figure 9). Such an interpretation is consistent with the differences between samples 1 and 2 in both laser-probe ages of phlogopite in strain fringes and in step-heated muscovite ages in matrix; as compared to sample 1, the significantly younger ages recorded for matrix muscovite in sample 2 are consistent with the generally younger ages recorded for strain fringe phlogopite in sample 2.

[43] Using equations of *Dodson* [1973], published diffusion data for muscovite, activation energy E = 217.6 kJ mol$^{-1}$ and frequency factor $D_o$ = 0.04 cm$^2$ s$^{-1}$ [*Hames and Bowring*, 1994], and analyzed grain size of 110 $\mu$m (average natural grain size, 60 $\mu$m; 25–125 $\mu$m range) with an infinite cylinder diffusion geometry for matrix muscovite, calculated $T_c$ varies from 320°C to 385°C for geologic cooling rates of 1–100°C Ma$^{-1}$. Thus, the $T_c$ for matrix muscovite is similar to estimated temperatures for phlogopite growth, and is also consistent with the partial thermal resetting interpretation (Figure 9). Assuming an initial

detrital age of $\sim$400–420 Ma (from the high-temperature steps of the age spectrum, Appendix C) and the above diffusion parameters, calculations suggest fractional $^{40}Ar*$ loss for sample 1 corresponding to the step heating data ($\sim$20–25%) are attained by $\sim$750 ka at a maximum deformation temperature of 350°C. More reasonable geologic timescales of 1–10 Ma predict significantly greater $^{40}Ar*$ loss than observed. Temperatures of $\sim$305–335°C reproduce the apparent fractional $^{40}Ar*$ loss on timescales of 1–10 Ma, consistent with the other geologic constraints on deformation temperatures.

[44] Several lines of evidence indicate that $T_c$ for phlogopite is significantly higher than those for biotite and muscovite [*Giletti*, 1974; *Dahl*, 1996; *Grove and Harrison*, 1996]. Using published diffusion parameters for phlogopite [*Giletti*, 1974], E = 242.3 kJ mol$^{-1}$ and $D_o$ = 0.75 cm$^2$ s$^{-1}$, an average strain fringe phlogopite width of 200 $\mu$m (perpendicular to $c$ axis), and cooling rates of 1–100°C Ma−1, calculated $T_c$ varies from 361°C to 430°C. Together with geologic constraints on deformation temperatures and apparent incomplete resetting of detrital muscovite, these observations substantiate the interpretation that the phlogopite ages from sample 1 represent growth ages, not cooling ages. Because the fibers are syntectonic with $D_1$, the ages therefore represent deformation ages.

[45] Similar arguments suggest that the muscovite laser-probe ages from the Black Pine Mountains also represent growth ages, not cooling ages. The assessment of metamorphic conditions during cleavage formation and strain fringe growth in the Black Pine Mountains is hindered by the polymetamorphic nature of the Mississippian siltite and slate into which the $\sim$144 Ma sills intrude. An early metamorphism is recorded by mineral assemblages in Mississippian slate including phengite-chlorite-chloritoid and andalusite-chloritoid-chlorite, and by conodont color alteration indices of 5–5.5 [*Christensen*, 1975; *Smith*, 1982; *Wells et al.*, 1990], which indicate metamorphic temperatures of $\sim$350–400°C; this metamorphism is interpreted to be synchronous with intrusion of the sills. A second metamorphism accompanied cleavage formation and the growth of quartz-muscovite strain fringes in slate and in the sills. Temperature estimates of 200–350°C for the second metamorphism are constrained by illite crystallinity determinations of the <2 um size fraction from argillite [*Wells et al.*, 1990]. These temperature conditions are consistent with the limited argon loss exhibited by the muscovite age spectra from the contact aureole (Figure 11), demonstrating that the temperatures during strain fringe growth were insufficient to cause significant volume diffusion of $^{40}Ar$ in muscovite. These observations suggest that the laser-probe ages of muscovite in the strain fringes from the Black Pine Mountains record ages of deformation and strain fringe growth, not cooling.

## 7.3. Tectonic Implications

[46] The $D_1$ fabric in the Raft River–Albion–Grouse Creek metamorphic core complex was previously suggested to record (1) oblique dextral thrusting during reactivation of a west-dipping thrust zone [*Malavieille*, 1987], and (2) gravitational spreading at the base of a thrust nappe [*Wells*, 1997]. This latter interpretation was based primarily on observations from the eastern Raft River Mountains including, general shear kinematics, deformation at metamorphic conditions, and the northeast trend to $L_1$, suggesting a possible link with eastward translation of thrust sheets within the Sevier foreland. Below we reevaluate the tectonic significance of the $D_1$ fabric on the basis of our more complete understanding of its age, regional distribution, and orientation.

[47] The kinematic significance of the $D_1$ fabric in Sevier orogenesis largely depends on the direction of $D_1$ flow with respect to the direction of shortening in the thrust belt; that is, does $D_1$ deformation transfer material eastward into the thrust belt, or is flow perpendicular to thrust transport? The Sevier fold-thrust belt is dominantly north trending, with salients and reentrants, and has traditionally been interpreted to record east-directed shortening [*Royse*, 1993; *Yonkee*, 1997] (Figure 1). The $L_1$ elongation lineation, taken as the flow direction, is dominantly N to NNE trending, despite variability in azimuth as great as 60° within and between structural plates (Figure 2). Furthermore, the rocks of the Black Pine Mountains and the Ordovician strata of the eastern Raft River Mountains, the two locations (Figure 2) where $L_1$ deviates most from a N trend (and that influenced the gravitational spreading hypothesis of *Wells* [1997]), lie in the upper plate of the Miocene Raft River detachment fault. Significant post-Cretaceous vertical axis rotations in the hanging wall of the detachment cannot be ruled out, thus we put more confidence in the lineation orientation within the basement parautochthon and within the structurally higher rocks west of the breakaway to the Raft River detachment (i.e., Grouse Creek Mountains), as representing the orientation of the Cretaceous $D_1$ fabric. North to NNE directed flow at midcrustal levels within the hinterland is predominantly parallel to the orogen, and nearly orthogonal to transport on major thrust sheets with 10s of kilometers of displacement in the foreland [*Royse*, 1993; *DeCelles*, 2004]. The kinematics of $D_1$ general shear flow and the resulting subhorizontal foliation and N-trending stretching lineation record subvertical shortening and N-S elongation. We reinterpret the $D_1$ fabric as recording synconvergent orogen-parallel extensional flow and reconcile below the development of this fabric within the hinterland of the fold-thrust belt dominated by eastward translation of thrust sheets.

[48] Synconvergent orogen-parallel extension is a common process in the interiors of orogens and has been interpreted within several tectonic contexts, including transpression resulting from oblique plate convergence [e.g., *Ellis and Watkinson*, 1987; *Mancktelow*, 1992; *McCaffrey*, 1992; *Murphy et al.*, 2002]; increased arcuation [e.g., *Ferranti et al.*, 1996; *Schmid et al.*, 1998]; collision with or without an indentor, causing lateral extrusion [e.g., *Tapponnier et al.*, 1982; *Kapp and Guynn*, 2004; *Rosenberg et al.*, 2004], and gravitational spreading resulting from unequal crustal thickening and/or erosional/extensional denudation along strike [e.g., *Coleman*, 1996]. While a salient in the frontal thrusts of the Sevier orogen exists to the east

of the study area (Idaho-Utah-Wyoming salient) (Figure 1), arcuation is inadequate to account for the magnitude $D_1$ strains; finite strain studies within the salient show strike-parallel extension magnitudes less than 10% [*Yonkee*, 2005], at least an order of magnitude less than the $D_1$ strain magnitudes. Collisional extrusion (in a strict sense) is also not viable for the Sevier hinterland as no mid-Cretaceous collisional events have been documented along the continental margin to the west.

[49] Much geologic and geophysical evidence indicates oblique plate convergence along the western margin of North America during the early and Late Cretaceous [*Lahren et al.*, 1990; *Greene and Schweickert*, 1995]. However, the mid-Cretaceous was apparently a time of nearly orthogonal plate convergence and shortening of the continental margin. Paleomagnetic plate reconstructions of the Mesozoic Pacific basin suggest that the Farallon and Kula plates, with respect to North America, underwent sinistral convergence during the Late Jurassic and early Cretaceous, dextral convergence during the Late Cretaceous, and orthogonal convergence in between [*Engebretson et al.*, 1985; *Kelley*, 1995]. The transitions, from sinistral to orthogonal to dextral convergence, originally estimated at ~120 and 105 Ma, respectively [*Engebretson et al.*, 1985], have been revised with newer relative plate motion and hot spot data to ~100 Ma and 83 Ma, respectively [*Kelley*, 1995]. These estimates favor dominantly orthogonal convergence during development of the ~105 Ma orogen-parallel lineation, but in consideration of the uncertainties, estimated at ±10 Ma (D. Engebreteson, personal communication, 2004), oblique convergence, based solely on the plate reconstructions, cannot be disproved.

[50] The 3-D geometry of the mid-Cretaceous $D_1$ strain fabric (subhorizontal foliation and N-trending stretching lineation) is difficult to interpret within the context of transpression. Vertical shortening and a low-angle foliation, as opposed to horizontal shortening and a high-angle foliation, requires one of several modifications to the classical transpressional model with straight, parallel-sided boundaries to the deformation zone [e.g., *Sanderson and Marchini*, 1984]: (1) oblique convergence along an arcuate plate margin [*Ave Lallemant and Guth*, 1990; *McCaffrey*, 1992; *McCaffrey and Nabelek*, 1998]; (2) systematic changes in convergence direction along a straight plate margin as a result of a pole of rotation close to the margin [*McCaffrey*, 1992]; (3) transtensional jogs within orogen-parallel strike-slip fault systems in otherwise transpressional orogens [*Murphy et al.*, 2002; *Mancktelow*, 1992]; (4) deformation within an "attachment zone" [*Tikoff et al.*, 2002], separating dextral translation of rigid upper-crustal blocks within the "orogenic float" [*Oldow et al.*, 1989] from deforming mantle lithosphere; or (5) low-angle boundary conditions resulting in inclined transpression.

[51] The mid Cretaceous Farallon–North America plate motions and geology of the Sevier orogen support none of the tectonic scenarios 1 to 5. Scenarios 3 and 4 require the existence of either unrecognized N-striking wrench faults in the hinterland or a significant and unrecognized wrench component to the frontal thrusts. Scenario 5 is implicit in the prior interpretation of *Malavieille* [1987] for $D_1$ as oblique dextral thrusting during reactivation of a west-dipping thrust zone. A preexisting low-angle anisotropy or rheological boundary may act as a strain guide and focus transpressional strain, but is seemingly energetically improbable. This is in contrast to the more common partitioning of oblique convergence into the orthogonal components of strike-slip motion along vertical zones of weakness, such as thermally softened magmatic arcs, and normal convergence along low-angle dipping zones including subduction zones and back arc thrusts [*Fitch*, 1972; *Beck*, 1983], such as occurred in the early and Late Cretaceous of the southern Cordilleran orogen [*Lahren et al.*, 1990; *Greene and Schweickert*, 1995].

[52] Subhorizontal foliation and orogen-parallel lineation within the mid Cretaceous hinterland are more compatible with extensional flow resulting from gravitational spreading than from transpression. The variability in lineation trend within the parauthochthon and between parauthochthon and allochthons (Figure 2) may be due to either variability in the orientation of extensional flow through time or coeval lateral and vertical variability in flow direction. Variability in azimuth of flow direction is common for gravitationally driven flow [e.g., *Camilleri*, 1998] as opposed to kinematics governed by plate convergence. While it is well recognized that the sinuous belt of metamorphic core complexes of western North America represents a significant crustal welt developed during Mesozoic crustal shortening [*Coney and Harms*, 1984], it is also probable that significant along-strike variations in crustal thickness developed, similar to ellipsoidal beads on a necklace, and that the core complexes represent these sites of greatest thickening. Such a variation in thickening along strike is recorded in the Ruby Mountain–East Humboldt Range–Wood Hills (Figure 1) where burial depths progressively increase from 3 kbars in the south to 9–10 kbars to the north [*Howard*, 2003, and references therein]. The upper-crustal analogy of localized thickening is well recognized in the development of structural culminations in fold-thrust belts, such as the Wasatch and Sevier culminations of the Sevier fold-thrust belt [*Yonkee*, 1992; *Mitra and Sussman*, 1997]. We interpret N-S flow as gravitational relaxation of ellipsoidal crustal welts resulting from mid crustal duplexing and development of culminations, triggered by thermal relaxation of tectonically thickened crust [*Camilleri*, 1998] (Figure 13). Flow parallel to the orogen is from regions of high toward low gravitational potential energy. E-W compression would impede orogen-perpendicular flow, and thus focus flow parallel to the orogen.

[53] Focused thrust burial and differential crustal thickening along strike may have been influenced by a significant crustal-scale discontinuity across the northeastern Great Basin. An approximately east-striking boundary separating Proterozoic rocks to the south from Archean rocks to the north extends from the Cheyenne Belt of southern Wyoming westward to the Ruby Mountains–East Humboldt Range of Nevada [*Bryant*, 1988; *Lush et al.*, 1988] (Figure 1). This boundary has been defined by isotopic studies of both younger magmatic rocks and of Precambrian
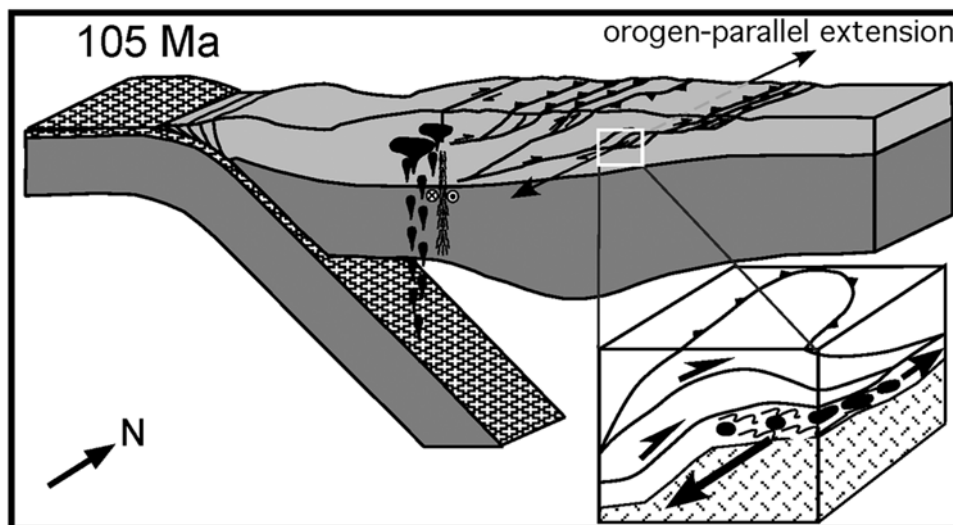
**Figure 13.** Tectonic model for development of orogen-parallel stretching and vertical shortening in the middle crust of the interior of the Sevier orogen. Inset shows constrictional strains at deep levels of structural culmination with lineation parallel to hinge lines of coeval folds.

basement [*Zartman*, 1974; *Lush et al.*, 1988; *Nelson et al.*, 2002]. Furthermore, stratigraphic studies have delineated an east-west trending zone, in otherwise north-trending facies boundaries, that represents the paleogeography of the Paleozoic shelf edge [*Miller et al.*, 1991] (Figure 1). The Precambrian crustal boundary may have influenced the geometry of the Late Precambrian rifted margin of western North America, such as developing linked normal and transform faults, and the geometry of the rifted margin may have influenced the paleogeography of the Paleozoic shelf edge. The position of the basement and/or facies boundaries probably focused crustal shortening through development of ramps and duplexes [*Miller et al.*, 1991; *Camilleri*, 1998].

[54] Orogen-parallel extension in the interior of the Sevier orogen, here constrained to 105 ± 6 Ma, is bracketed by, and was perhaps coeval with, major episodes of motion on thrusts in the fold-thrust belt. Shortening in the fold-thrust belt is largely constrained by dated synorogenic sedimentary rocks in wedge-top and foredeep basins [*Wiltschko and Dorr*, 1983; *Heller et al.*, 1986; *DeCelles*, 1994, 2004]. Motion on the Willard thrust, the oldest and westernmost thrust of the fold-thrust belt at this latitude (Figure 1), was initiated by 120–110 Ma (Ephraim Conglomerate [*Wiltschko and Dorr*, 1983; *Heller et al.*, 1986]). Renewed slip on the Willard thrust and slip on the Meade thrust are recorded in deposition of Aptian to Albian (115–100 Ma) deposits [*DeCelles*, 1994, 2004]. Early motion on the Crawford thrust began at ~90 Ma [*DeCelles*, 2004] and postdates the episode of orogen-parallel extension documented here.

## 8. Conclusions

[55] We have successfully dated in situ micas in two occurrences of fibrous strain fringes in greenschist-facies metamorphic rocks by the $^{40}Ar/^{39}Ar$ method, using both UV and $CO_2$ laser-probe techniques. Phlogopite was dated in quartz-calcite-phlogopite strain fringes from the Grouse Creek Mountains using both the UV and $CO_2$ laser probes; muscovite was dated in quartz-muscovite strain fringes from the Black Pine Mountains using the $CO_2$ laser probe. For the Grouse Creek samples, average ages for individual strain fringes range from 92 Ma to 110 Ma, with the most reliable ages from UV laser analyses of sample 1 ranging from 101 Ma to 110 Ma. The mean of the ages from sample 1 (105.0 ± 5.8 Ma), as well as an isochron obtained from analyses of sample 1, constrain the most reliable age to ~105 Ma, thus constraining the timing of $D_1$ deformation to the mid-Cretaceous. Analyses from sample 2 are considered less reliable owing to proximity to the Middle detachment and resultant deformation and incipient alteration. Analysis of muscovite in strain fringes from the nearby Black Pine Mountains using the $CO_2$ laser probe corroborates the results from sample 1 of the Grouse Creek Mountains, yielding a mean age of ~104.7 ± 5.8 Ma. Individual $CO_2$ laser-probe muscovite ages for 6 strain fringes range from 93 Ma to 117, and mean ages for the 6 strain fringes range from 97 Ma to 112 Ma.

[56] The analyses from the Grouse Creek and the Black Pine Mountains each represent the first successful application of the laser-probe $^{40}Ar/^{39}Ar$ dating method to in situ fibrous strain fringes. This promising result demonstrates that, with sufficiently low line blanks, high-K mineral phases of large enough size, strain fringes as young as mid-Cretaceous, and potentially younger, can be directly dated by the $^{40}Ar/^{39}Ar$ laser-probe technique. The $CO_2$ laser, which provides larger sample gas yields, may prove useful in some cases wherein the target phase is encased in non-K-bearing phases such as quartz and these can be shown to contribute insignificant amounts of argon.

[57] The mid-Cretaceous ages for the strain fringes represent deformation ages and date an episode of orogen-

parallel extension in the interior of the Sevier orogenic wedge. Orogen-parallel extension in the Sevier orogen may be more common than currently recognized, and other candidates for Cretaceous N-S flow include the New York Mountains of the eastern Mojave Desert [*Burchfiel and Davis*, 1977; *Smith et al.*, 2003] and the Ruby Mountains–East Humboldt Range–Wood Hills [*MacCready et al.*, 1997; *Camilleri*, 1998], although the separation of Cretaceous from Eocene-Miocene deformation is sometimes difficult owing to kinematic reactivation. Mid-Cretaceous N-S flow is spanned by major episodes of motion on the Willard and Crawford thrusts of the fold-thrust belt, and thus may have been synchronous with continued shortening. Synconvergent gravitational spreading, parallel to orogenic strike, of localized crustal welts produced by midcrustal duplexing, provides a viable tectonic explanation.

# References

Armstrong, R. L. (1968), Mantled gneiss domes in the Albion Range, southern Idaho, *Geol. Soc. Am. Bull.*, *79*, 1295–1314, doi:10.1130/0016-7606(1968)79[1295:MGDITA]2.0.CO;2.

Armstrong, R. L. (1976), The geochronology of Idaho (Part 2), *Isochron West*, *15*, 1–33.

Ave Lallemant, H. G., and L. R. Guth (1990), Role of extensional tectonics in exhumation of eclogites and blueschists in an oblique subduction setting: Northern Venezuela, *Geology*, *18*, 950–953, doi:10.1130/0091-7613(1990)018<0950:ROETIE>2.3.CO;2.

Beck, M. E. (1983), On the mechanism of tectonic transport in zones of oblique subduction, *Tectonophysics*, *93*, 1–11, doi:10.1016/0040-1951(83)90230-5.

Berman, R. G. (1988), Internally-consistent thermodynamic data for minerals in the system $Na_2O-K_2O-CaO-MgO-FeO-Fe_2O_3-Al_2O_3-SiO_2-TiO_2-H_2O-CO_2$, *J. Petrol.*, *29*, 445–522.

Bryant, B. (1988), Geology of the Farmington Canyon Complex, Wasatch Mountains, Utah, *U.S. Geol. Surv. Prof. Pap.*, 1476, 54 pp.

Burchfiel, B. C., and G. A. Davis (1977), Geology of the Sagamore Canyon–Slaughterhouse Spring area, New York Mountains, California, *Geol. Soc. Am. Bull.*, *88*, 1623–1640, doi:10.1130/0016-7606(1977)88<1623:GOTSCS>2.0.CO;2.

Camilleri, P. A. (1998), Prograde metamorphism, stain evolution, and collapse of footwalls of thick thrust sheets, a case study from the Mesozoic Sevier hinterland, U.S.A, *J. Struct. Geol.*, *20*, 1023–1042, doi:10.1016/S0191-8141(98)00032-7.

Camilleri, P. A., and K. R. Chamberlain (1997), Mesozoic tectonics and metamorphism in the Pequop Mountains and Wood Hills region, northeast Nevada: Implications for the architecture and evolution of the Sevier orogen, *Geol. Soc. Am. Bull.*, *109*, 74–94.

Cebula, G. T., M. J. Kunk, H. H. Mehnert, C. W. Naeser, J. D. Obradovich, and J. F. Sutter (1986), The Fish Canyon Tuff, a potential standard for the $^{40}Ar$-$^{39}Ar$ and fission-track dating methods (abstract), *Terra Cognita*, *6*, 139.

Christensen, O. D. (1975), Metamorphism of the Manning Canyon and Chainman Formations, Ph.D. thesis, 194 pp, Stanford Univ., Palo Alto, Calif.

Coleman, M. E. (1996), Orogen-parallel and orogen-perpendicular extension in the central Nepalese Himalayas, *Geol. Soc. Am. Bull.*, *108*, 1594–1607.

Compton, R. R. (1972), Geologic map of Yost quadrangle, Box Elder County, Utah, and Cassia County, Idaho, *U. S. Geol. Surv. Misc. Geol. Invest Map*, *I-672*, 1 p.

Compton, R. R. (1975), Geologic map of Park Valley quadrangle, Box Elder County, Utah, and Cassia County, Idaho, *U. S. Geol. Surv. Misc. Geol. Invest. Map*, *I-873*, 1 p.

Compton, R. R., V. R. Todd, R. E. Zartman, and C. W. Naeser (1977), Oligocene and Miocene metamorphism, folding, and low-angle faulting in northwestern Utah, *Geol. Soc. Am. Bull.*, *88*, 1237–1250, doi:10.1130/0016-7606(1977)88<1237:OAMMFA>2.0.CO;2.

Coney, P. J., and T. Harms (1984), Cordilleran metamorphic complexes: Cenozoic extensional relics of Mesozoic compression, *Geology*, *12*, 550–554, doi:10.1130/0091-7613(1984)12<550:CMCCCE>2.0.CO;2.

Dahl, P. (1996), The crystal chemical basis for Ar retention in micas: Inferences from interlayer partitioning and implications for geochronology, *Contrib. Mineral. Petrol.*, *123*, 22–39, doi:10.1007/s004100050141.

DeCelles, P. G. (1994), Late Cretaceous-Paleocene synorogenic sedimentation and kinematic history of the Sevier thrust belt, northeast Utah and southwest Wyoming, *Geol. Soc. Am. Bull.*, *106*, 32–56, doi:10.1130/0016-7606(1994)106<0032:LCPSSA>2.3.CO;2.

DeCelles, P. G. (2004), Late Jurassic to Eocene evolution of the Cordilleran thrust belt and foreland basin system, western U.S.A, *Am. J. Sci.*, *304*, 105–168, doi:10.2475/ajs.304.2.105.

Di Vincenzo, G., R. Carosi, and R. Palmeri (2004), The relationship between tectono-metamorphic evolution and argon isotope records in white mica: Constraints from in situ $^{40}Ar$-$^{39}Ar$ laser analysis of the Varsican basement of Sardinia, *J. Petrol.*, *45*, 1013–1043, doi:10.1093/petrology/egh002.

Dodson, M. H. (1973), Closure temperature in cooling geochronological and petrological systems, *Contrib. Mineral. Petrol.*, *40*, 259–274, doi:10.1007/BF00373790.

Dunlap, W. J. (1997), Neocrystallization or cooling? $^{40}Ar/^{39}Ar$ ages of white micas from low-grade mylonites, *Chem. Geol.*, *143*, 181–203, doi:10.1016/S0009-2541(97)00113-7.

Ellis, M., and A. J. Watkinson (1987), Orogen-parallel extension and oblique tectonics: The relation between stretching lineations and relative plate motion, *Geology*, *15*, 1022–1026, doi:10.1130/0091-7613(1987)15<1022:OEAOTT>2.0.CO;2.

Engebretson, D. C., A. Cox, and R. G. Gordon (1985), Relative motions between oceanic and continental plates in the Pacific Basin, *Spec. Pap. Geol. Soc. Am.*, *206*, 59 pp.

Ferranti, L., J. S. Oldow, and M. Sacchi (1996), Pre-Quaternary crustal extension in the Southern Apennine belt, Italy: Arcuation and orogen-parallel collapse, *Tectonophysics*, *260*, 325–347, doi:10.1016/0040-1951(95)00209-X.

Fitch, J. T. (1972), Plate convergence, transcurrent faults, and internal deformation adjacent to Southeast Asia and the Western Pacific, *J. Geophys. Res.*, *77*, 4432–4460, doi:10.1029/JB077i023p04432.

Getty, S. R., and L. P. Gromet (1992), Geochronological constraints on ductile deformation, crustal extension, and doming about a basement-cover boundary, New England Appalachians, *Am. J. Sci.*, *292*, 359–397.

Giletti, B. J. (1974), Studies in diffusion 1: Argon in phlogopite mica, in *Geochemical Transport and Kinetics, Publ. 634*, edited by A. W. Hofmann, pp. 107–115, Carnegie Inst., Washington, D. C.

Greene, D. C., and R. A. Schweickert (1995), The Gem Lake shear zone: Cretaceous dextral transpression in the northern Ritter Range pendant, eastern Sierra Nevada, California, *Tectonics*, *14*, 945–961, doi:10.1029/95TC01509.

Grove, M., and T. M. Harrison (1996), $^{40}Ar*$ diffusion in Fe-rich biotite, *Am. Mineral.*, *81*, 940–951.

Hames, W. E., and S. A. Bowring (1994), An empirical evaluation of the argon diffusion geometry in muscovite, *Earth Planet. Sci. Lett.*, *124*, 161–167, doi:10.1016/0012-821X(94)00079-4.

Harris, C. R., T. D. Hoisch, and M. L. Wells (2007), Construction of a composite pressure-temperature path: Revealing the synorogenic burial and exhumation history of the Sevier hinterland, USA, *J. Metamorph. Geol.*, *25*, 915–934.

Heller, P. L., S. S. Bowdler, H. P. Chambers, J. C. Coogan, E. S. Hagen, M. W. Shuster, N. S. Winslow, and T. F. Lawton (1986), Time of initial thrusting in the Sevier orogenic belt, Idaho-Wyoming and Utah, *Geology*, *14*, 388–391, doi:10.1130/0091-7613(1986)14<388:TOITIT>2.0.CO;2.

Hoisch, T. D., M. L. Wells, and L. M. Hanson (2002), Pressure-temperature paths from garnet zoning: Evidence for multiple episodes of thrust burial in the hinterland of the Sevier orogenic belt, *Am. Mineral.*, *87*, 115–131.

Howard, K. A. (2003), Crustal structure in the Elko-Carlin region, Nevada, during Eocene gold mineralization: Ruby-East Humboldt metamorphic core complex as a guide to the deep crust, *Econ. Geol.*, *98*, 249–268, doi:10.2113/98.2.249.

Jordan, T., B. Isacks, R. Allmendinger, J. Brewer, V. Ramos, and C. Ando (1983), Andean tectonics related to the geometry of the subducted plate, *Geol. Soc. Am. Bull.*, *94*, 341–361, doi:10.1130/0016-7606(1983)94<341:ATRTGO>2.0.CO;2.

Kapp, P., and J. H. Guynn (2004), Indian punch rifts Tibet, *Geology*, *32*, 993–996.

Kelley, K. P. (1995), Relative motions between North America and oceanic plates of the Pacific basin during the last 130 million years, M.S. thesis, Western Wash. Univ., Bellingham.

Kerrick, D. M., and C. K. Jacobs (1981), A modified Redlich-Kwong equation for $H_2O$, $CO_2$, and $H_2O$-$CO_2$ mixtures at elevated pressures and temperatures, *Am. J. Sci.*, *28*, 735–767.

Koehn, D., C. Hilgers, P. D. Bons, and C. W. Passchier (2000), Numerical simulation of fibre growth in antitaxial strain fringes, *J. Struct. Geol.*, *22*, 1311–1324, doi:10.1016/S0191-8141(00)00039-0.

Lahren, M. M., R. A. Schweickert, J. M. Mattinson, and J. D. Walker (1990), Evidence of uppermost Proterozoic to Lower Cambrian miogeoclinal rocks and the Mojave-Snow Lake fault: Snow Lake pendant, central Sierra Nevada, California, *Tectonics*, *9*, 1585–1608, doi:10.1029/TC009i006p01585.

Lush, A. P., A. J. McGrew, A. W. Snoke, and J. E. Wright (1988), Allochthonous Archean basement in the northern East Humboldt Range, Nevada, *Geology*, *16*, 349–353, doi:10.1130/0091-7613(1988)016<0349:AABITN>2.3.CO;2.

MacCready, T., A. W. Snoke, J. E. Wright, and K. A. Howard (1997), Mid-crustal flow during Tertiary extension in the Ruby Mountains core complex, Nevada, *Geol. Soc. Am. Bull.*, *109*, 1576–1594, doi:10.1130/0016-7606(1997)109<1576:MCFDTE>2.3.CO;2.

Malavieille, J. (1987), Kinematics of compressional and extensional ductile shearing deformation in a metamorphic core complex of the northeastern Basin and Range, *J. Struct. Geol.*, *9*, 541–554, doi:10.1016/0191-8141(87)90139-8.

Mancktelow, N. S. (1992), Neogene lateral extension during convergence in the Central Alps: Evidence from interrelated faulting and backfolding around the Simplonpass (Switzerland), *Tectonophysics*, *215*, 295–317, doi:10.1016/0040-1951(92)90358-D.

McCaffrey, R. (1992), Oblique plate convergence, slip vectors, and forearc deformation, *J. Geophys. Res.*, *97*, 8905–8915, doi:10.1029/92JB00483.

McCaffrey, R., and J. Nabelek (1998), Role of oblique convergence in the active deformation of the Himalayas and southern Tibet plateau, *Geology*, *26*, 691–694, doi:10.1130/0091-7613(1998)026<0691:ROOCIT>2.3.CO;2.

McGrew, A. J., M. T. Peters, and J. E. Wright (2000), Thermobarometric constraints on the tectonothermal evolution of the East Humboldt Range metamorphic core complex, Nevada, *Geol. Soc. Am. Bull.*, *112*, 45–60, doi:10.1130/0016-7606(2000)112<0045:TCOTTE>2.3.CO;2.

Miller, D. M. (1980), Structural geology of the northern Albion Mountains, south-central Idaho, *Mem. Geol. Soc. Am.*, *153*, 399–423.

Miller, D. M., J. E. Repetski, and A. G. Harris (1991), *East-trending Paleozoic continental margin near Wendover, Utah, Publ. 67*, pp. 439–461, Pac. Sect., Soc. Econ. Paleontol. Mineral., Tulsa, Okla.

Mitra, G., and A. J. Sussman (1997), Structural evolution of connecting splay duplexes and their implications for critical taper: An example based on geometry and kinematics of the Canyon Range culmination, Sevier Belt, central Utah, *J. Struct. Geol.*, *19*, 503–521, doi:10.1016/S0191-8141(96)00108-3.

Morrison, J., and J. L. Anderson (1998), Footwall refrigeration along a detachment fault: Implications for the thermal evolution of core complexes, *Science*, *279*, 63–66, doi:10.1126/science.279.5347.63.

Mulch, A., and M. A. Cosca (2004), Recrystallization or cooling ages: In situ UV-laser $^{40}$Ar/$^{39}$Ar geochronology of muscovite in mylonitic rocks, *J. Geol. Soc.*, *161*, 573–582, doi:10.1144/0016-764903-110.

Mulch, A., M. A. Cosca, and H. R. Handy (2002), In-situ UV-laser $^{40}$Ar/$^{39}$Ar geochronology of a micaceous mylonite: An example of defect-enhanced argon loss, *Contrib. Mineral. Petrol.*, *142*, 738–752.

Mulch, A., M. A. Cosca, A. Andresen, and J. Fiebig (2005), Time scales of deformation and exhumation in extensional detachment systems determined by high-spatial resolution in situ UV-laser $^{40}$Ar/$^{39}$Ar dating, *Earth Planet. Sci. Lett.*, *233*, 375–390, doi:10.1016/j.epsl.2005.01.042.

Müller, W. (2003), Strengthening the link between geochronology, textures and petrology, *Earth Planet. Sci. Lett.*, *206*, 237–251, doi:10.1016/S0012-821X(02)01007-5.

Müller, W., D. Aerden, and A. N. Halliday (2000), Isotopic dating of strain fringe increments: Duration and rates of deformation in shear zones, *Science*, *288*, 2195–2198, doi:10.1126/science.288.5474.2195.

Murphy, M. A., A. Yin, P. Kapp, T. M. Harrison, C. E. Manning, F. J. Ryerson, D. Lin, and G. Jinghui (2002), Structural evolution of the Gurla Mandhata detachment system, southwest Tibet: Implications for the eastward extent of the Karakoram fault system, *Geol. Soc. Am. Bull.*, *114*, 428–447, doi:10.1130/0016-7606(2002)114<0428:SEOTGM>2.0.CO;2.

Nelson, S. T., R. A. Harris, M. J. Dorais, M. Heizler, K. N. Constenius, and D. E. Barnett (2002), Basement complexes in the Wasatch fault, Utah, provide new limits on crustal accretion, *Geology*, *30*, 831–834, doi:10.1130/0091-7613(2002)030<0831:BCITWF>2.0.CO;2.

Oldow, J. S., A. W. Bally, H. G. Av'e Lallemant, and W. P. Leeman (1989), Phanerozoic evolution of the North American Cordillera: United States and Canada, in *The Geology of North America: An Overview*, edited by A. W. Bally and A. R. Palmer, pp. 139–232, *Geol. Soc. of Am.*, Boulder, Colo.

Ramsay, J. G., and M. L. Huber (1983), *The Techniques of Modern Structural Geology, 1: Strain Analysis*, 307 pp., Academic Press, London.

Reddy, S. M., and G. J. Potts (1999), Constraining absolute deformation ages: the relationship between deformation mechanisms and isotope systematics, *J. Struct. Geol.*, *21*, 1255–1265, doi:10.1016/S0191-8141(99)00032-2.

Reddy, S. M., S. P. Kelley, and J. Wheeler (1996), A $^{40}$Ar/$^{39}$Ar laser probe study of micas from the Sesia Zone, Italian Alps: Implications for metamorphic and deformation histories, *J. Metamorph. Geol.*, *14*, 493–508, doi:10.1046/j.1525-1314.1996.00338.x.

Rejebian, V. A., A. G. Harris, and J. S. Huebner (1987), Conodont color and textural alteration: An index to regional metamorphism, contact metamorphism, and hydrothermal alteration, *Geol. Soc. Am. Bull.*, *99*, 471–479, doi:10.1130/0016-7606(1987)99<471:CCATAA>2.0.CO;2.

Roberts, H. J., S. P. Kelley, and P. S. Dahl (2001), Obtaining geologically meaningful $^{40}$Ar-$^{39}$Ar ages from altered biotite, *Chem. Geol.*, *172*, 277–290, doi:10.1016/S0009-2541(00)00255-2.

Rosenberg, C. L., J. P. Brun, and D. Gapais (2004), Indentation model of the Eastern Alps and the origin of the Tauern Window, *Geology*, *32*, 997–1000, doi:10.1130/G20793.1.

Royse, F. (1993), An overview of the geologic structure of the thrust belt in Wyoming, northern Utah, and eastern Idaho, *Geol. Surv. Wyoming Mem.*, *5*, 272–311.

Rutter, E. H. (1983), Pressure solution in nature, theory and experiment, *J. Geol. Soc.*, *140*, 725–740, doi:10.1144/gsjgs.140.5.0725.

Sanderson, D., and R. D. Marchini (1984), Transpression, *J. Struct. Geol*, *6*, 449–458, doi:10.1016/0191-8141(84)90058-0.

Schmid, S. M., T. Berza, V. Diaconescu, N. Froitzheim, and B. Fugenschuh (1998), Orogen-parallel extension in the Southern Carpathians, *Tectonophysics*, *297*, 209–228, doi:10.1016/S0040-1951(98)00169-3.

Sheely, J. C. (2002), Kinematics and timing of normal faulting in a metamorphic core complex: Grouse Creek Mountains, Utah, MS thesis, 146 pp., Univ. of Nev., Las Vegas.

Sherlock, S. C., S. P. Kelley, J. A. Zalasiewicz, D. I. Schofield, J. A. Evans, R. J. Merriman, and S. J. Kemp (2003), Precise dating of low-temperature deformation: Strain-fringe analysis by $^{40}$Ar-$^{39}$Ar laser microprobe, *Geology*, *31*, 219–222, doi:10.1130/0091-7613(2003)031<0219:PDOLTD>2.0.CO;2.

Smith, A. G., M. L. Wells, and D. Foster (2003), Timing and development of an orogen-parallel lineation and of frontal thrusting in the southern Cordilleran fold-thrust belt, New York Mountains, California, *Geol. Soc. Am. Abstr. Programs*, *35*, 513.

Smith, J. F. (1982), Geologic map of the Strevell 15 minute quadrangle, Cassia County, Idaho, *Map I-1403*, scale 1:62500, U. S. Geol. Surv., Boulder, Colo.

Steven, T. A., H. H. Mehnert, and J. D. Obradovich (1967), Age of volcanic activity in the San Juan Mountains, Colorado, *U. S. Geol. Surv. Prof. Pap.*, *575-D*, 47–55.

Tapponnier, R., G. Peltzer, A. Y. Le Dain, R. Armijo, and P. Cobbold (1982), Propagating extrusion tectonics in Asia: New insights from simple experiments with plasticine, *Geology*, *10*, 611–616, doi:10.1130/0091-7613(1982)10<611:PETIAN>2.0.CO;2.

Tikoff, B., C. Teyssier, and C. Waters (2002), Clutch tectonics and the partial attachment of lithospheric layers, in *Continental Collision and the Tectono-Sedimentary Evolution of Forelands, Stephan Mueller Spec. Publ. Ser.*, vol. 1, edited by G. Bertotti, K. Schulmann, and S. A. P. L. Cloetingh, pp. 57–73, Eur. Geosci. Union, Strasbourg, France.

Todd, V. R. (1980), Structure and petrology of a Tertiary gneiss complex in northwestern Utah, *Mem. Geol. Soc. Am.*, *153*, 349–383.

Wells, M. L. (1997), Alternating contraction and extension in the hinterlands of orogenic belts: An example from the Raft River Mountains, Utah, *Geol. Soc. Am. Bull.*, *109*, 107–126, doi:10.1130/0016-7606(1997)109<0107:ACAEIT>2.3.CO;2.

Wells, M. L., and R. W. Allmendinger (1990), An early history of pure shear in the upper plate of the Raft River metamorphic core complex; Black Pine Mountains, southern Idaho, *J. Struct. Geol.*, *12*, 851–868, doi:10.1016/0191-8141(90)90059-8.

Wells, M. L., R. D. Dallmeyer, and R. W. Allmendinger (1990), Late Cretaceous extension in the hinterland of the Sevier thrust belt, northwestern Utah and southern Idaho, *Geology*, *18*, 929–933, doi:10.1130/0091-7613(1990)018<0929:LCEITH>2.3.CO;2.

Wells, M. L., T. D. Hoisch, L. Hanson, J. Struthers, and E. Wolfe (1997), Large magnitude crustal thickening and repeated extensional exhumation in the Raft River, Grouse Creek, and Albion Mountains, *Brigham Young Univ. Geol. Stud.*, *42*, 325–340.

Wells, M. L., T. D. Hoisch, M. P. Peters, D. M. Miller, E. W. Wolff, and L. W. Hanson (1998), The Mahogany Peaks Fault, a Late Cretaceous-Early Paleocene normal fault in the hinterland of the Sevier Orogen, *J. Geol.*, *106*, 623–634.

Wendt, I., and D. Carl (1991), The statistical distribution of the mean squared weighted deviation, *Chem. Geol.*, *86*, 275–285.

Wijbrans, J. A., and I. McDougall (1986), $^{40}$Ar/$^{39}$Ar dating of white micas from an Alpine high-pressure metamorphic belt on Naxos (Greece): The resetting of the argon isotopic system, *Contrib. Mineral. Petrol.*, *93*, 187–194, doi:10.1007/BF00371320.

Wiltschko, D. V., and J. A. Dorr (1983), Timing of deformation in overthrust belt and foreland of Idaho, Wyoming, and Utah, *Am. Assoc. Pet. Geol. Bull.*, *67*, 1304–1322.

Yonkee, W. A. (1992), Basement-cover relations, Sevier orogenic belt, northern Utah, *Geol. Soc. Am. Bull.*, *104*, 280–302, doi:10.1130/0016-7606(1992)104<0280:BCRSOB>2.3.CO;2.

Yonkee, W. A. (1997), Kinematics and mechanics of the Willard thrust sheet, central part of the Sevier orogenic wedge, north-central Utah, *Brigham Young Univ. Geol. Stud.*, *42*, 341–354.

Yonkee, W. A. (2005), Strain patterns within part of the Willard thrust sheet, Idaho-Utah-Wyoming thrust belt, *J. Struct. Geol.*, *27*, 1315–1343, doi:10.1016/j.jsg.2004.06.014.

Zartman, R. E. (1974), Lead isotopic provinces of the Cordillera of the western United States and the geologic significance, *Econ. Geol.*, *69*, 792–805.

————————
T. Arriola, T. L. Spell, M. L. Wells, and K. A. Zanetti, Department of Geoscience, University of Nevada, Las Vegas, 4505 Maryland Parkway, Las Vegas, NV 89154-4010, USA. (michael.wells@unlv.edu)

T. D. Hoisch, Department of Geology, Northern Arizona University, Box 4099, Flagstaff, AZ 86011, USA.